JGR Oceans

RESEARCH ARTICLE
10.1029/2024JC021293

Groundwater Hydrodynamic Oscillations From Swash With Transparent Sand (GHOSTS)

Delaney M. Benoit[1], Marie-Pierre C. Delisle[2,3], Greg Siemens[4], Britt Raubenheimer[2], Steve Elgar[2], and Ryan P. Mulligan[1]

[1]Department of Civil Engineering, Queen's University, Kingston, ON, Canada, [2]Woods Hole Oceanographic Institution, Woods Hole, MA, USA, [3]United States Naval Academy, Annapolis, MD, USA, [4]Royal Military College of Canada, Kingston, ON, Canada

Key Points:

- Transparent sand and optically matched fluid are used to investigate swash zone subsurface dynamics experimentally
- The relationship between waves, runup, and subsurface saturation are scaled to dimensionless parameters
- Three cross-shore location-dependent regimes are defined for subsurface fluid elevation profiles in a beach

Correspondence to:
D. M. Benoit,
delaney.benoit@queensu.ca

Citation:
Benoit, D. M., Delisle, M.-P. C., Siemens, G., Raubenheimer, B., Elgar, S., & Mulligan, R. P. (2025). Groundwater hydrodynamic oscillations from swash with transparent sand (GHOSTS). *Journal of Geophysical Research: Oceans*, *130*, e2024JC021293. https://doi.org/10.1029/2024JC021293

Received 1 MAY 2024
Accepted 15 FEB 2025

Author Contributions:
Conceptualization: Delaney M. Benoit, Marie-Pierre C. Delisle, Greg Siemens, Ryan P. Mulligan
Formal analysis: Delaney M. Benoit, Marie-Pierre C. Delisle, Greg Siemens, Britt Raubenheimer, Ryan P. Mulligan
Methodology: Delaney M. Benoit, Marie-Pierre C. Delisle, Greg Siemens, Ryan P. Mulligan
Software: Delaney M. Benoit, Greg Siemens
Supervision: Ryan P. Mulligan
Validation: Delaney M. Benoit
Visualization: Delaney M. Benoit, Greg Siemens
Writing – original draft: Delaney M. Benoit
Writing – review & editing: Delaney M. Benoit, Marie-Pierre C. Delisle, Greg Siemens, Britt Raubenheimer, Steve Elgar, Ryan P. Mulligan

Abstract Interactions between surface flows and groundwater in beaches can influence erosion and accretion, wave overtopping, groundwater levels and salinization, and transport of nutrients and pollutants. Laboratory experiments using transparent crushed quartz and optically matched mineral oil as proxies for sand and water allow the degree of saturation to be computed at pore-scale (0.7 mm resolution) enabling detailed investigations of the wave runup driven infiltration into a beach in a wave flume for a range of slopes and flow boundary conditions. The evolution of the wetting front resulting from wave runup on an initially unsaturated beach is described in detail, including the formation of an infiltration wedge in the subsurface of the swash zone and the wave-driven rise in fluid elevation inside the beach. The elevation of the runup for each event is found to be related closely to the saturation of the beach face, reaching an equilibrium state once the subsurface in the swash zone reaches capacity. The back wall boundary condition in the flume has a significant role in how subsurface flows increase saturation within the beach, especially with boundary head elevations greater than the initial phreatic surface. The results of these novel experimental observations are used to develop dimensionless relationships between the surface wave runup and the subsurface saturation rates. To improve monitoring and interpretation of future coastal groundwater studies, three distinct cross-shore regimes are defined for assessing change in subsurface fluid elevation in the beach.

Plain Language Summary During storms, waves that break on shorelines can drive surface water into the ground. In this study, transparent sand and mineral oil are used to enable continuous observations of fluid flow in the subsurface in space and time. In a set of experiments, the transparent sand is used to study how fluids enter, exit, and move throughout a beach as waves break and runup across the surface. As waves runup an initially dry beach surface, fluid flows into the beach and forms a wedge-shaped wet region. After the waves break, the distance the fluid travels up the beach face is found to be related closely to the saturation of the beach below the breaking wave, which changes over time until the beach is at a maximum saturation and the runup distance is constant. Boundary control at the end of the beach impacts the elevation of the fluid in the back of the beach, especially when the boundary condition is at a greater elevation than the fluid in the beach. Three distinct regions in a beach are defined based on the subsurface fluid elevation regimes to improve approaches for measuring changes to coastal groundwater systems.

1. Introduction

Sandy beaches comprise 31% of the earth's non-ice coastline and have a critical role in the dynamic interactions that occur between the ocean and groundwater at the land-sea interface (Luijendijk et al., 2018). Infiltration and exfiltration of ocean water into beaches affects the transport of surface sediments, and thus beach erosion and accretion (Bond et al., 2023; Butt et al., 2001; Sous et al., 2013; Turner & Masselink, 1998). These processes also can affect the landward extent of ocean surface waves, influencing overtopping and flooding (Delisle et al., 2023). Seepage processes in beaches can affect coastal groundwater salinization and the exchange of nutrients and pollutants between the aquifer and ocean (Boufadel et al., 2007; Cantelon et al., 2022; Cartwright et al., 2004; Gast et al., 2015; Geng et al., 2021; Nielsen, 1999; Werner et al., 2013). Further, groundwater depletion is contributing to the evolution of coastal environments as aquifers are pumped at rates higher than can be replenished, altering ambient groundwater levels and subsurface flows (Wada et al., 2016). The magnitudes and importance of these processes is determined by the ocean, sediment, and aquifer properties (Geng et al., 2021; Heiss et al., 2022; Waska et al., 2019).

Understanding the processes occurring in the swash zone, the intermittently submerged region of the beach between the maximum wave runup and most seaward wave run-down (Raubenheimer & Guza, 1996), is especially important as sea-level rise will cause higher mean water elevations and wave runup. Within the swash zone, complex and interacting hydrodynamic processes occur, including free surface flows along the beach face (uprush, backwash), infiltration and exfiltration fluxes, and groundwater flow within nearshore aquifers (Robinson et al., 2006, 2007a; Santos et al., 2012). The beach subsurface can be divided into the phreatic (saturated) zone and the vadose (unsaturated) zone, separated by an interface of granular material with atmospheric pore pressures (the phreatic surface or groundwater table). As the swash zone moves shoreward and seaward with the tide, the ambient groundwater table fluctuates in elevation, with the groundwater table rising faster than it falls due to the low slope of natural beaches (Austin & Masselink, 2006; Nielsen, 1990). This asymmetry in infiltration and exfiltration results in a groundwater table that is higher than the tidally averaged ocean water level (an overheight or bulge). Surface water losses owing to vertical infiltration into permeable beaches can reduce the surface runup elevation (Delisle et al., 2023). Storms and large-wind events can cause rapid increases in runup and surge, forcing a response in the beach subsurface (Robinson et al., 2014). During intense storms, the groundwater level in the beach can increase by more than 1 m, forming a bulge in groundwater that can propagate several hundred meters inland over a few days (Housego et al., 2021).

During swash, lower frequency oscillations of the groundwater-table exit point (the intersection of the phreatic surface and the beach face) drives decoupling between the groundwater and the surface water, allowing for enhanced infiltration when runup is landward of the exit point and increased exfiltration along the beach when the swash is seaward of the exit point (Austin & Masselink, 2006; van Gent, 1994). Infiltration and exfiltration modify the thickness of the surface wave bottom boundary layer and alter the near-bed velocities and shear stresses, which may be more pronounced in dry beaches with low water tables (Conley & Inman, 1994; Grant, 1948; Waddell, 1976). The effective weight of sediments also can increase during runup owing to downward-directed pressure gradients (and flows) that stabilize the bed, whereas the upwards-directed pressure gradients (and flows) during run-down can destabilize the bed after flow reversal (Bond et al., 2023; Butt et al., 2001; Florence et al., 2022; Turner & Masselink, 1998). Infiltration-driven wave boundary layer thinning and the resulting increases in shear stresses and loss of surface water owing to infiltration into dry sediments both can increase swash asymmetry and drive onshore transport of sediment in the upper swash, although the relative dominance of these processes is grain-size dependent (Austin & Masselink, 2006; Bond et al., 2023; Butt et al., 2001; Florence et al., 2022; Masselink & Li, 2001; Turner & Masselink, 1998). Infiltration and exfiltration flows are larger on coarser sand beaches compared with finer beaches, and thus may have a greater effect on accretion and erosion (Bakhtyar et al., 2011).

Tide- and storm-driven groundwater table elevations and circulation result from vertical fluxes of water through the beach (Turner et al., 2016; Waddell, 1976). Swash-driven infiltration on a steep, high-permeability gravel beach has been described using a "dual pathway model," with two modes of subsurface saturation: (a) infiltration at the exit point that elevates the groundwater table and propagates across the phreatic surface as a wave; and (b) vertical gravity-driven infiltration through the unsaturated beach that flows downwards to intersect the phreatic surface at a swash-lagged rate (Austin & Masselink, 2006). Maximum infiltration into the unsaturated gravel beach occurs shortly after the wave arrival, causing water content near the beach surface to increase rapidly, which then declines to zero during rundown as water propagates downwards within the subsurface (Heiss et al., 2014, 2015; Kikkert et al., 2013). For random waves with a broad range of frequencies, as on many natural beaches, low-frequency fluctuations may dominate the infiltration processes in the upper swash (Sous et al., 2013). Saturation deeper in the beach is initially dominated by a rise in the groundwater table, which gradually intersects with the runup-driven wetting front to form the infiltration wedge (or saturated mound) with entrapped air that migrates shoreward in sandy beaches (Heiss et al., 2015; Yang et al., 2022). The relative importance of each infiltration mechanism may depend upon grain size and beach permeability (Austin & Masselink, 2006; Heiss et al., 2015; Turner et al., 2016; Yang et al., 2022). Increased permeability allows greater volumes of fluid to infiltrate into the void spaces of the beach, resulting in greater losses of water from the surface waves and reduced runup elevations relative to those on less permeable beaches (Delisle et al., 2023). In highly permeable environments, such as gravel beaches, runup can infiltrate rapidly into the unsaturated region and induce near instantaneous oscillations in groundwater elevation near the swash zone (Austin & Masselink, 2006). The saturation of the subsurface also can alter the relative infiltration capacity of the beach and fine-grained

beaches that become saturated quickly and drain slowly can experience less infiltration with each runup event (Duncan, 1964; van Gent, 1994; Packwood, 1983).

The rate of downward movement of the wetting front depends on beach permeability (Geng et al., 2017). Trapped pore air reduces the infiltration rate through the vadose zone (Siemens et al., 2014), inhibits movement of the wetting front, and impacts fluxes of ambient groundwater, especially for finer grained sediments. As the beach becomes saturated from successive waves, the groundwater bulge that forms in the upper swash zone creates a subsurface flow divergence, directing upper beach groundwater flows inland and mid and lower beach groundwater flows seaward (Kang et al., 1994; Sous et al., 2013; Turner et al., 2016; Yang et al., 2022). Fluctuations in the groundwater table are more pronounced for coarser sediments (Bakhtyar et al., 2011). The capillary fringe, the region that forms above the saturated zone due to capillary forces (negative pore pressures), is an important determinant of groundwater response to infiltration (Geng et al., 2017; Horn, 2002; Li et al., 1997; Yang et al., 2022; Zheng et al., 2023), and depends on the beach sediment properties. The negative pore pressures in the capillary fringe cause groundwater to seep upwards into sediment pore spaces, which enables more rapid rises of the groundwater table elevation in response to runup infiltration. Entrapped air, which limits the water capacity in granular pore spaces and can alter groundwater flow paths, as well as infiltration and exfiltration rates, is impacted by the beach permeability (Constantz et al., 1988; Faybishenko, 1995; Horn, 2002, 2006). Flows within the swash zone also are sensitive to the heterogeneity of the granular media (Geng et al., 2020). Thus, the hydrological and geological processes on a beach are coupled closely.

Observations of small-scale swash-groundwater interaction processes may be constrained by the spatial density of in-situ sensors that can be deployed without disturbing the hydrodynamic processes. Laser-induced fluorescence and particle image velocimetry have been used to observe infiltration under swash from a dam-break-like bore (Steenhauer et al., 2011). However, more common are point measurements, primarily collected with wells or piezometers for low frequency oscillations and buried pressure transducers or probes for higher frequency measurements, which may miss discrete changes in saturation and fluid transport between instrument locations. Remote sensing of groundwater properties is possible at coarse (regional and global) scales and is not applicable to fine scale observations (Adams et al., 2022). Subsurface air entrapment is measured with individual sensors or by collecting sediment samples, primarily providing data at selected discrete locations (Horn, 2002). Non-intrusive, high-resolution measurement techniques are necessary to advance understanding of the highly complex swash zone.

The interactions between surface runup and the beach subsurface fluid influences many geophysical processes. Swash-driven infiltration is an important process that drives changes to erosion and accretion by altering bottom boundary layer thickness and bed stability (Austin & Masselink, 2006; Bond et al., 2023; Butt et al., 2001; Florence et al., 2022; Masselink & Li, 2001; Turner & Masselink, 1998). Further, the sediment properties of a beach can have important implications for the infiltration and exfiltration rates, groundwater table response, and sediment transport (Bakhtyar et al., 2011; Butt et al., 2001; Geng et al., 2017). Understanding the mechanisms that drive infiltration into a beach can advance predictions of beach evolution and subsurface response. Here, a novel set of physical model experiments is performed to provide pore-scale observations (down to 0.7 mm) of the interactions between continuous surface wave-driven runup and groundwater flow in an unconfined, homogeneous nearshore aquifer. The approach overcomes the limitations of in-situ probe measurements by using crushed fused quartz sand and an optically matched fluid (i.e., identical refractive indices), where the quartz is transparent at 100% saturation and opaque when dry. A description of the transparent sand, experimental setup and data processing approach applied to convert digital videos to degree of saturation images at pore-scale resolution are provided. High spatiotemporal resolution laboratory test results are presented and analyzed to determine wave runup and subsurface fluid responses for different flume boundary conditions and beach slopes. The physical model results provide new insight into how varying beach slopes and boundary conditions, controlled by a valve and a head tank with adjustable fluid elevation at the back wall boundary, influence the wave runup and subsurface fluid response. An overview of the potential applications of the findings of this surface-ground fluid interaction study to field scales are discussed, including a conceptual model of subsurface fluid elevation regimes that relate infiltration progression to cross-shore location.

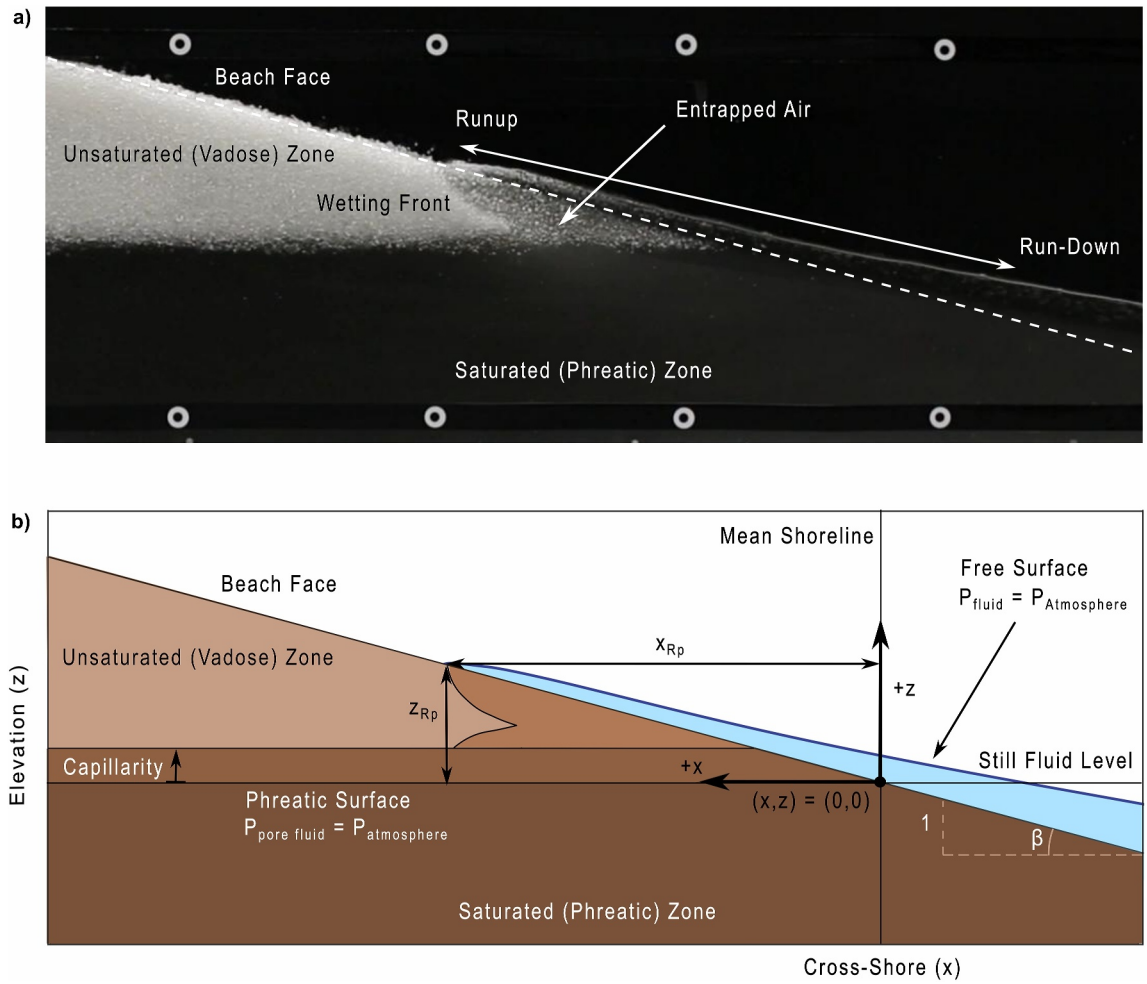

Figure 1. Side view of wave runup and subsurface flow processes in a beach: (a) sample unprocessed image on a 1:4 beach slope with coarse-grained transparent sand, and (b) diagram showing the coordinate system and important variables. The white dashed line in (a) identifies the beach face, which is invisible below the still water line as the fully saturated grains optically disappear in front of the black background.

2. Methods

2.1. Transparent Sand

Fused quartz, which appears transparent when saturated with an optically matched oil mixture, is used to visualize and quantify high-resolution spatiotemporal changes in the degree of pore saturation as swash from periodic surface waves saturate the beach (Figure 1). Transparent sand has been used for a variety of geotechnical research applications, including investigating 3-dimensional groundwater flows, the role of entrapped air in subsurface flows, soil deformation, and geosynthetics (Ganiyu et al., 2016; Siemens et al., 2014; Sills et al., 2017). Here, transparent sand is used to investigate the interactions between free surface and subsurface flows through porous media in a beach subjected to surface waves.

The material properties used in transparent sand studies have been well documented (Ezzein & Bathurst, 2011; Munson et al., 1998; Peters et al., 2011). The sediment used is a crushed fused quartz, available in two uniformly graded grain sizes, coarse-grained sand (D_{50} = 1.7 mm) and fine-grained sand (D_{50} = 0.4 mm) (Peters et al., 2011). A mineral oil mixture is designed to match the quartz refractive index of 1.459. The oil mixture has a density of 0.845 g/cm^3 and a dynamic viscosity of 10.1 cP at 25°C. A full description of the sediment properties of the fine- and coarse-grained quartz are provided in Siemens et al. (2014). Here, tests are primarily performed using the coarse-grained sand, with one additional test performed using the fine-grained sand (Section 3.4).

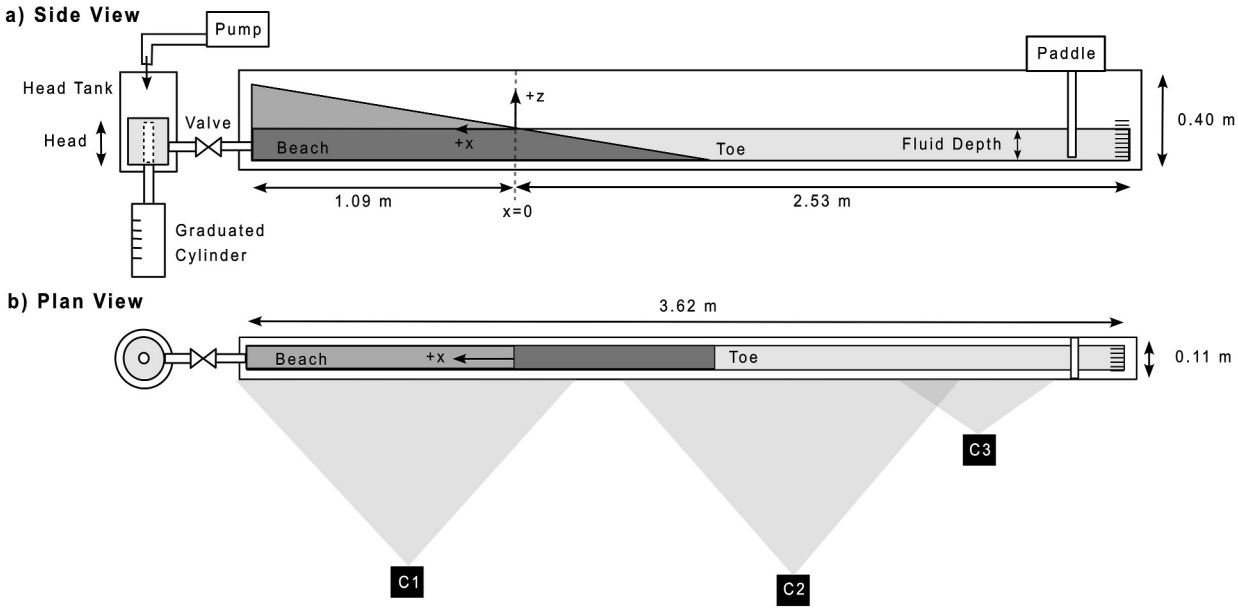

Figure 2. Experimental set-up: (a) side view, and (b) plan view of the flume configuration for the 1:6 slope. Waves are generated by the paddle (right) and propagate to the beach (left). Behind the beach, a valve connects the flume to a head tank with a standpipe for overflow drainage into a graduated cylinder and pump to maintain the head if fluid leaves the system. The field of view for cameras C1, C2, and C3 are shown. The beach toe is at $x = -78$ cm for 1:6 slopes and $x = -52$ cm for 1:4 slopes.

An important feature of this material combination is the identical refractive indices. When the quartz is 100% saturated by the oil mixture, the materials appear homogenous. Within the oil-quartz mixture, interstitial air between grains can be observed, allowing air entrapment between grains to be quantified and the migrating wetting front within the subsurface to be tracked. Unprocessed camera imagery of the material mixture has a range of brightness, including the dark saturated zone and the opaque (near white) unsaturated zone, as well as the gray zone with interstitial air trapped by fluid below the wave runup (Figure 1a). Although the opaque white unsaturated portion of the beach appears to float above the phreatic surface, the saturated and unsaturated regions are one continuous granular material with and without the pores filled with the oil mixture.

The quartz-oil mixture has been analyzed (Peters et al., 2011; Sills et al., 2017) to map the local variation in digital image intensity with degree of saturation (S_r), which quantifies the presence of interstitial pore air. After image processing, pixel intensity of the transparent sand is converted to a saturation scale ranging from $S_r = 0$ for dry material to $S_r = 1$ for fully saturated material, enabling discrete pixel-by-pixel quantification of the degree of saturation across the domain. Image processing of transparent sand experiments are beneficial for studying spatially dependent processes, because pore-scale data can be obtained with high-resolution digital cameras (discussed in Section 2.3).

The transparent sand and high-viscosity oil mixture do not replicate exactly the interactions between sand and lower-viscosity water. Rather, these materials are applied here to investigate infiltration and subsurface flows between fluid and porous media, which can be used to form connections to sand-water exchanges. Transparent sand has potential for obtaining a detailed understanding of processes and flow pathways, but should not be extended beyond its practical limitations.

2.2. Experimental Set-Up

Experiments are performed in a 40 cm deep, 11 cm wide, and 362 cm long wave flume constructed of 1.7 cm thick transparent acrylic (Perspex) (Figure 2). The right end wall of the flume includes a smooth acrylic motorized wave paddle mounted on guiding tracks that transforms rotational motion into horizontal translational movements, generating waves to propagate from right (offshore) to left (onshore) onto the beach. The paddle span is 15.4 cm and the offshore wall of the flume has dampening material to minimize wave reflection. The maximum crest elevation and the beach toe position are dependent on the slope of a given test, whereas the cross-shore intersection of the still fluid level and the mean shoreline is constant for all cases. The back wall (onshore) contains a

Table 1
Summary of Experimental Conditions With Coarse-Grained Quartz

Test	Slope	Valve state	Boundary head, h	Waves
1–3	1:6	Closed	-	On
4–6	1:6	Open	13 cm	On
7–9	1:6	Open	17 cm	On
10	1:6	Open	17 cm	Off
11–13	1:6	Open	21 cm	On
14	1:6	Open	21 cm	Off
15–17	1:4	Closed	-	On
18–20	1:4	Open	13 cm	On
21–23	1:4	Open	17 cm	On
24	1:4	Open	17 cm	Off
25–27	1:4	Open	21 cm	On
28	1:4	Open	21 cm	Off

drainage port centered 2 cm above the bottom of the flume that can be closed or opened. The mouth of the port is fitted with a fine mesh that allows the passage of oil, but not granular material and provides flow resistance at the boundary. This port is attached to a constant head tank with an adjustable standpipe. When the fluid level within the head tank exceeds the standpipe elevation, overflow drains into a graduated cylinder. The head tank also features a pump to maintain the fluid level within the tank if fluid flows into the flume. The front side wall of the flume is framed by white circles on a black background for use as geo-referencing points for image analysis.

The experiments use the oil mixture described in Section 2.1, and thus the stationary fluid depth (previously still water level) is described as the "still fluid level" and the elevation of fluid within the subsurface (previously groundwater table) is described as the "phreatic surface" within the beach. The cross-shore coordinates increase in the direction of wave propagation from the paddle (right, offshore) to the beach (left, onshore) and the vertical elevation is defined as positive upwards. The still fluid level is defined as elevation $z = 0$. Due to capillary rise, the subsurface fluid initially is elevated 2.3–3.6 cm above the still fluid level. The mean shoreline is where the still fluid level intersects the beach face, defined as cross-shore position $x = 0$. The origin ($x = 0$, $z = 0$) is at the intersection of the still fluid level and the beach surface (Figure 1b). The free surface, initially the same as the still fluid level at $t = 0$, denotes the moving interface between the surface fluid and the atmosphere. Runup is defined as the positive cross-shore movement of the free surface up the beach face ($+x$, $+z$) and run-down is the negative cross-shore movement of the free surface down the beach face ($-x$, $-z$). The vertical and cross-shore coordinates are normalized by the steady state runup elevation, z_{Rp}, and the steady state cross-shore runup, x_{Rp}, for each test (Section 3.1). The wetting front is the region of new saturation above the phreatic zone within the beach and below the beach face in the initial vadose zone.

Tests are performed for different combinations of constant beach slope (1:6, which is angle $\beta = 9.5°$; or 1:4, $\beta = 14.0°$), valve state (open or closed), and boundary head conditions ($h = 13$, 17, or 21 cm) (Table 1). Beach slopes are varied to investigate the impacts of beach profile on runup elevation, swash infiltration, and wetting front progression, and are selected based on constraints of the flume dimensions and sediment angle of repose. Boundary conditions with different head elevations are included to incorporate the interactions of swash-driven infiltration with other flows within a beach, such as an elevated phreatic surface moving seaward. All tests are performed with a still fluid depth of $d_0 = 13$ cm and monochromatic waves (shown at two locations in Figure 3), with wave period $T = 1.25$ s (frequency $f = 0.80$ Hz) and wave height $H = 7$ cm at $x = -200$ cm near the wave paddle. After generation, waves (Figure 3a) propagate toward the beach, shoal (Figure 3b), and break onto the beach face. The cameras are used to observe the wave mean and maximum vertical free surface fluid depths at cross-shore locations in each image (Figure 4). As waves propagate, the mean free surface elevation (η_{mean}) decreases below the still fluid level (wave set-down) before wave set-up on the beach slope (blue curve in Figure 4b). The maximum free surface elevation (η_{max}, green curve in Figure 4b) increases as waves propagate onshore until breaking ($x > -20$ cm) and then runup on the beach. The runup elevation of each wave, z_R, roughly is constant on the 1:6 slope, but is variable at the start of the test on the 1:4 slope and reaches steady-state after the first four to five waves (Figure 5, discussed further in Section 3.1). The bathymetry evolves during the experiment and is reshaped between tests. Bathymetric changes are similar for tests with the same beach slope.

The valve connecting the back wall behind the beach to the head tank is used in both open and closed positions to investigate the impacts on the beach when subsurface fluid flow horizontally is confined or unconfined. When the valve is opened, a range of unconfined aquifer conditions can be simulated by adjusting the height (h) of the standpipe in the attached head tank. Three heights are tested: $h = 13$ cm to investigate a continuous ambient phreatic surface behind the beach ($h = d_0$), and $h = 17$ or 21 cm to recreate a charged inland aquifer, similar to many natural coastal systems. Tests with a head tank elevation equal to the still fluid depth ($h = d_0$) start with the valve open and fluid at rest. For tests with a standpipe height above the still fluid level ($h > d_0$), the valve is opened at the beginning of the test to avoid flow from the head tank into the flume prior to the start of the test. Similarly, the valve is closed at the end of the test to prevent additional drainage after the waves are stopped. In tests with the valve in the open position, fluid can flow in and out of the flume. Net fluid flow out of the flume (fluid losses of

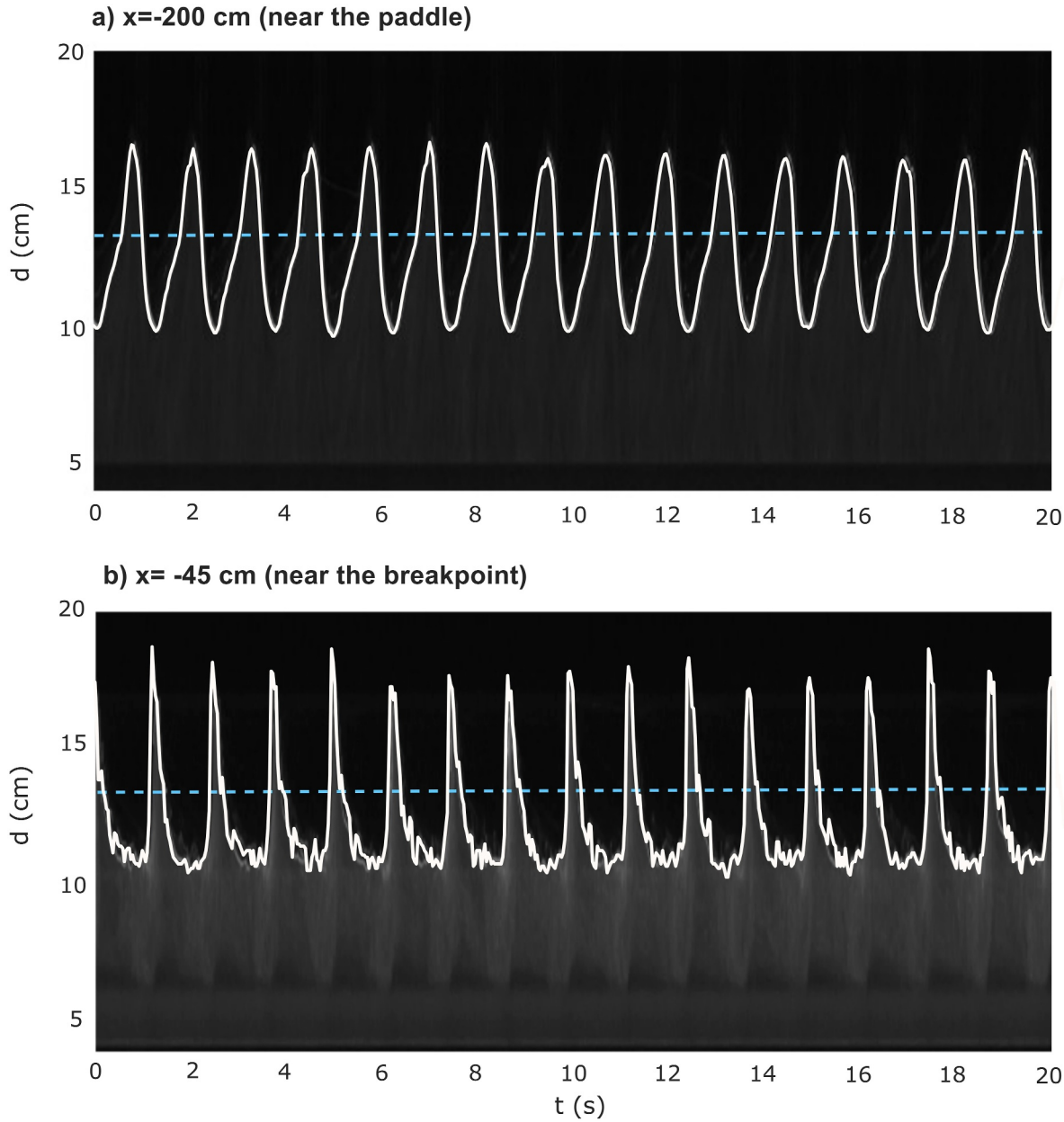

Figure 3. Fluid free surface elevation (white curve) vs. time from camera images for a 1:4 beach slope test: (a) near the wave paddle ($x = -200$ cm) from camera C3, and (b) on the beach before the breakpoint ($x = -45$ cm) from camera C2. Still fluid level ($d_0 = 13$ cm) is indicated by the blue dashed line.

<1% of the initial flume volume) occurs for $h = 13$ cm head tank conditions due to a wave-driven fluid bulge within the subsurface that moves toward the back of the flume. Under elevated head conditions ($h = 17$ or 21 cm), fluid flows into the flume from the head tank. The volume of fluid that enters the flume depends on the relative head of the boundary condition. When fluid is flowing into the flume ($h > d_0$), the pump is used to transport fluid into the head tank at a constant rate and a standpipe drains any overflow fluid into a graduated cylinder.

To observe the progression of the wetting front, tests are conducted for 1,200–1,800 s following the generation of the first wave from the paddle. The number of waves, or dimensionless time t/T, is defined as the time since arrival of the first wave to the beach toe divided by the wave period ($T = 1.25$ s). Three replicate tests are performed for each combination of beach slope, valve state, and boundary head conditions to observe repeatability. Additionally, one control test without any waves is run for each boundary head elevation ($h > d_0$) on each slope to

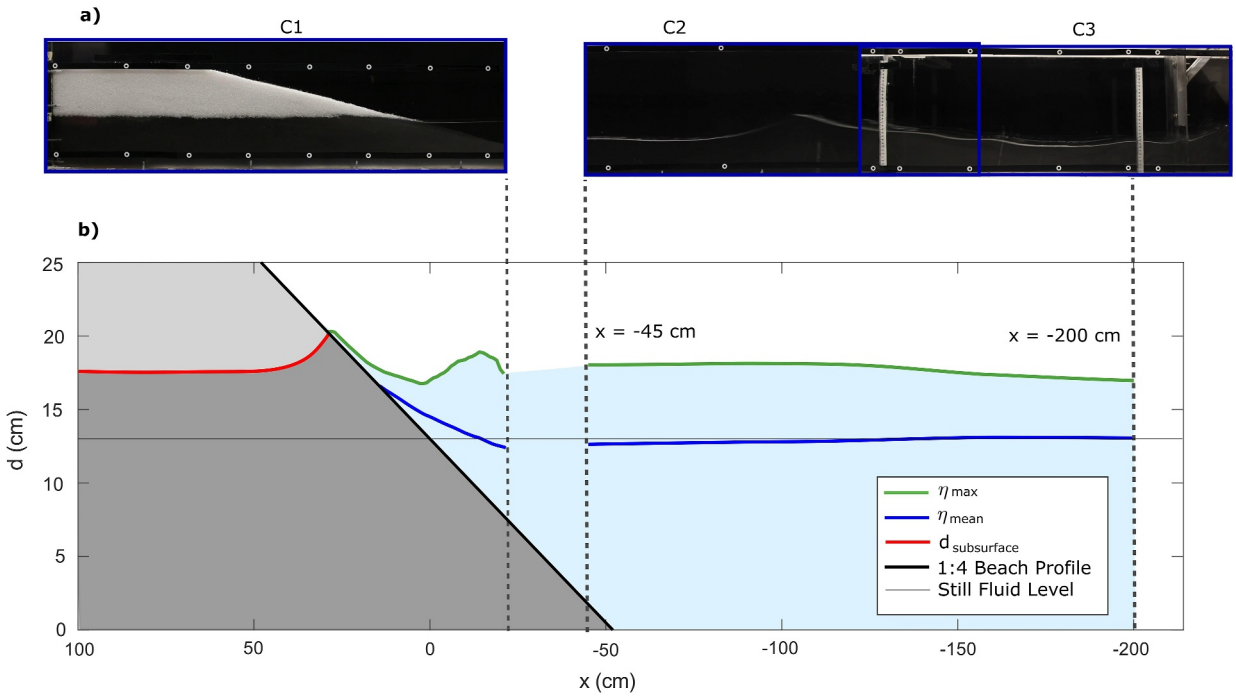

Figure 4. Fluid elevations from surface to subsurface: (a) sample images from each camera used to detect the fluid surface elevation, and (b) depth versus cross-shore distance along the flume including the mean free surface ($\eta_{mean,}$ blue curve) and the maximum free surface (η_{max}, green curve) measured over 1,200 s. The subsurface fluid height ($d_{subsurface}$, red curve) is shown for the end of the test. The beach slope is 1:4 with the closed valve boundary condition and the still fluid level is $d_0 = 13$ cm (Test 15). The vertical dashed lines indicate the locations shown in Figure 3a ($x = -200$ cm) and 3b ($x = -45$ cm). Note the gap in camera coverage between C1 and C2 ensures that images from C1 are not impacted from reflections or shadows caused by C2.

isolate and observe fluid flow from the head tank into the flume. Between experiments, the wave paddle is turned off and the beach is drained to achieve equilibrium fluid levels between the surface and subsurface.

Three cameras (Figure 2b) mounted on tripods record videos of the flume at 30 frames per second with 1,920 × 1,080 pixel resolution. Camera 3 (C3, Canon Rebel T6) images a close-up view of wave generation near the paddle. Camera 2 (C2, Canon Rebel T6) records a wide field of view of the flume, extending from the paddle to the wave breaking zone. Camera 1 (C1, Canon Mark III) images wave shoaling, breaking, and runup, as well as the extent of the granular subsurface to the beach wall, and is used to examine infiltration in the swash zone. A gap in camera coverage between C1 and C2 ensures that images from C1 are not impacted from reflections or shadows caused by C2. The side wall of the flume (behind the fluid) is painted black to provide contrast with the white opaque color of dry transparent sand. In the surrounding laboratory area, white sheets are placed behind the flume to reduce shadows and image background noise, and black sheets are placed behind the cameras to minimize reflection from the acrylic flume walls.

2.3. Digital Image Processing

Camera C1 obtains images with a pixel resolution of 0.7 mm and is set up with optimal spatial resolution to prevent over- and under-resolving data (Siemens & Beddoe, 2017). To avoid over-resolved observations, the resolution of a digital image (i.e., the pixel size) of granular material should not be smaller than the actual size of grains and pores. If too few pixels are used to image the granular material, the data no longer are representative of the subsurface (Siemens & Beddoe, 2017). Here, the pixel size (0.7 mm) is smaller than the grain size (1.7 mm), and therefore the images are averaged over five pixels (px) in the x- and z-directions, giving a resolution of 3.5 mm/px.

The high-resolution videos are processed to visualize wetting front migration and to quantify the degree of saturation (Peters et al., 2011; Sills et al., 2017). The videos are separated into individual images and are spatially rectified using GeoPIV (White et al., 2003), which identifies the locations of geo-referencing points and corrects for any camera movement, and aligns the dry and saturated images with each test image prior to image

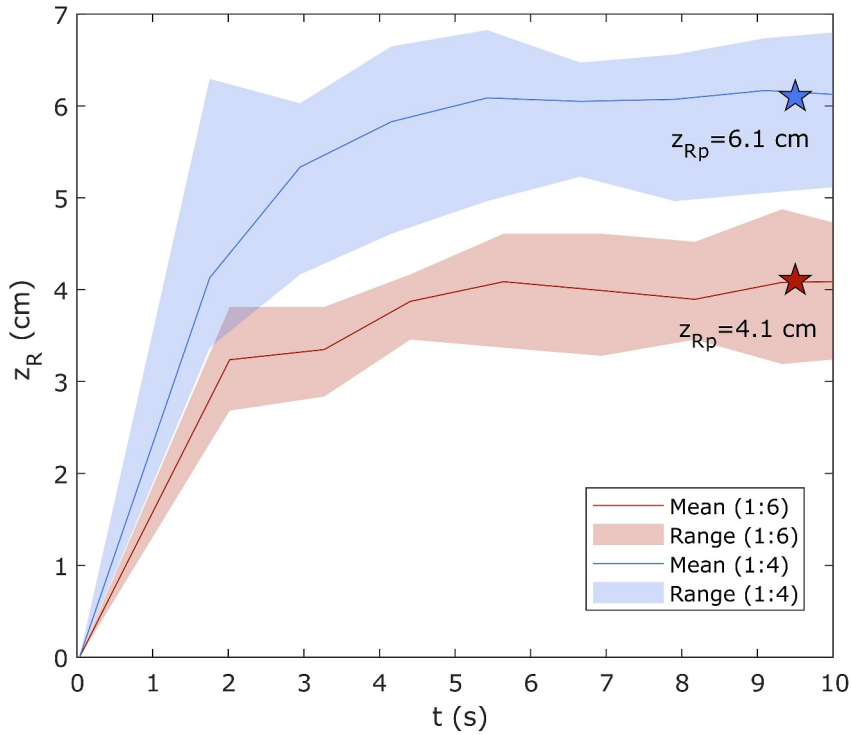

Figure 5. Vertical runup elevation, z_R, above the still fluid level for individual waves over 10 s for 1:4 (blue colors) and 1:6 (red colors) beach slopes versus time. Solid curves indicate the mean runup elevation and shading represents the range of runup elevations observed over 12 tests on each slope. The steady state runup elevation, z_{Rp}, for each beach slope is indicated with a star.

subtraction. Each test image is converted to gray-scale and the normalized intensity is computed at the pixel scale, relative to the saturated and dry control images (Figure 6), using:

$$I_N(x,z) = \frac{I_D(x,z) - I(x,z)}{I_D(x,z) - I_S(x,z)} \quad (1)$$

For each frame and at each x-z pixel coordinate, I_N is the computed normalized pixel intensity, I_D is the pixel intensity of the dry image, I is the pixel intensity of the image in gray scale, and I_S is the pixel intensity of the saturated image.

Compared with previous studies, a modification to the image processing method was made by replacing the dry image (transparent sand that never has contacted oil) with a "residual saturation" image to maintain consistency of the granular material for the control images. Transparent sand that has been used in prior laboratory tests maintains a small amount of residual saturation even after being drained of oil. Although these grains appear dry, they retain consistent residual normalized intensity ($I_{Nr} = 0.07 \pm 0.01$) and residual degree of saturation values ($S_{rr} = 0.05 \pm 0.003$) (Sills et al., 2017). To account for this difference, after input into Equation 1, normalized intensity values are linearly scaled from the range of 0–1.0 (I_N) to 0.07–1.0 (I_{Nr}). For each pixel normalized intensity, the degree of saturation (S_r) is calculated as (Sills et al., 2017):

$$S_r(x,z) = \left\{ \frac{-0.95}{\ln(0.07)} \ln(I_{Nr}(x,z)) \right\} + 1 \quad (2)$$

The result of this image processing is a set of images that quantify the degree of saturation ($S_r = 0$–1) on a linear black-to-white scale (Figure 6).

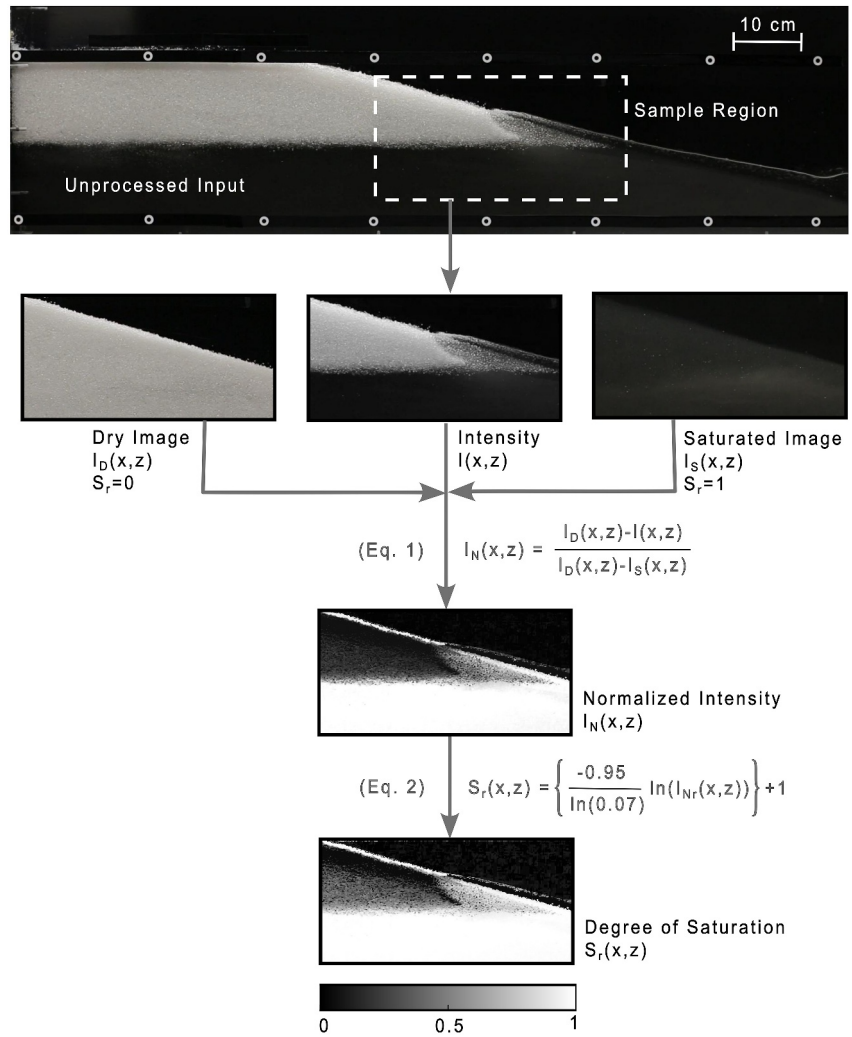

Figure 6. Steps in the image processing workflow. Processing begins with an unprocessed true color image (top), and a selected sample region to be processed shown by the dashed box. Next, a dry (completely unsaturated) calibration image and a fully saturated calibration image are used to compute the normalized intensity of the sample image after conversion to greyscale using Equation 1. Then, the normalized image is converted to show the degree of saturation (bottom) on a scale that ranges from 0 to 1.0 using Equation 2.

3. Results

All results and discussion focus on tests using coarse-grained transparent sand (D_{50} = 1.7 mm), with limitations discussed in Section 3.4.

3.1. Runup Elevation

The beach slope plays a significant role in maximum runup elevation (Kang et al., 1994; Li & Raichlen, 2001; Raubenheimer & Guza, 1996; Stockdon et al., 2006). Here, the runup elevation in the swash zone varies between the two beach slopes, where waves on the steeper 1:4 beach runup higher than those on the 1:6 beach (Figure 5). Runup elevations on the steeper beach increase during the first 4–5 waves (t = 5–7 s) and reach steady state by t = 10 s between z_R = 5.1–6.8 cm. Runup elevation on the flatter 1:6 slope remains approximately constant in time between z_R = 3.3–4.6 cm. The mean runup elevation across all tests on each beach slope is used to define a steady state runup elevation, z_{Rp}, for each slope (indicated with stars in Figure 5). Although these values indicate higher steady state runup distance on the steeper beach (z_{Rp} = 6.1 cm for 1:4 slope) than the more gently sloping beach

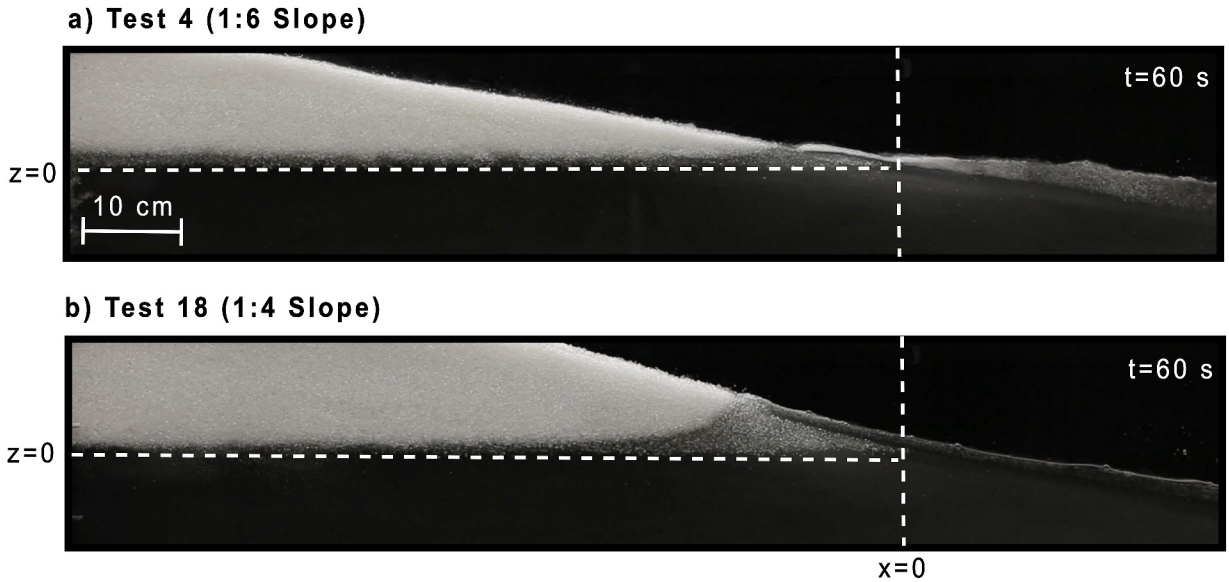

Figure 7. Unprocessed images of the wetting front at $t = 60$ s ($t/T = 48$) for (a) Test 4, 1:6 slope, and (b) Test 18, 1:4 slope (Table 1). The still fluid level ($z = 0$) and the mean shoreline ($x = 0$) are indicated by horizontal and vertical dashed lines, respectively.

($z_{Rp} = 4.1$ cm for 1:6 slope), the steady state horizontal runup distance is approximately the same for both slopes, $x_{Rp} = \sim 24.5$ cm.

The saturation of the beach face greatly decreases the hydraulic conductivity of the granular material (Constantz et al., 1988; Faybishenko, 1995) and the infiltration capacity. Once the infiltration wedge reaches its maximum saturation for a given test, the runup elevation remains steady. Prior to infiltration wedge saturation ($t < 5$ s in Figure 5), more vertical infiltration may be occurring in the upper swash. Thus, when runup is infiltrating into the dry beach face at elevations above the phreatic surface, thinning of the boundary layer may be stronger and the velocities and shear stresses at the bed could be increased for coarser grain sizes ($D_{50} > 1.5$ mm) (Conley & Inman, 1994; Waddell, 1976).

In this two-dimensional (x, z) study that idealizes the swash zone with cross-shore and vertical fluxes only, the alongshore movement of fluid is neglected. The incident waves are normal to the beach and runup and run-down are confined to the same x–z plane. Therefore, this laboratory experiment cannot replicate field conditions with shore-oblique waves and alongshore movement of runup, run-down, and subsurface flows. This setup therefore also neglects the escape of trapped pore air in the alongshore direction.

3.2. Infiltration Wedge

In all tests the infiltration wedge forms in the initially unsaturated zone of the beach below the horizontal wave runup and above the phreatic surface. The formation of this wedge occurs when $t/T = \sim 24$, where $t/T = 0$ indicates the arrival of the first wave to the beach toe. Although the shape of the runup-driven wedge is variable between tests on different beach slopes (Figure 7), the shape and size of the wedge is consistent across triplicate tests with the same conditions. For a test on 1:4 slope with coarse-grained sand and the valve closed, for $t/T = 0$–48 (the first 60 s), the runup drives vertical infiltration into the beach, which forms a propagating wetting front in the subsurface that saturates a wedge-shaped region below the surface wave runup (Figure 8). The brightness of this region indicates air entrapment within the wedge ($0 < S_r < 1$). Consistent with prior results (Austin & Masselink, 2006; Heiss et al., 2015; Yang et al., 2022), changes in saturation occur in the upward direction from the phreatic zone at the same time as in the downward direction due to infiltration from the beach face, forming a backwards "C" shaped wetting front that fills in over time between $x/x_{Rp} = 0$ and 1. After $t/T = \sim 24$, the infiltration wedge reaches steady-state and saturation changes are isolated to $x/x_{Rp} > 1$ (discussed in Section 3.3). Further, after formation of the infiltration wedge, the exit point maintains a constant location at the approximate coordinates of the peak runup (x_{Rp}–z_{Rp}), and remains decoupled from the free surface swash (a seepage face with enhanced exfiltration during rundown).

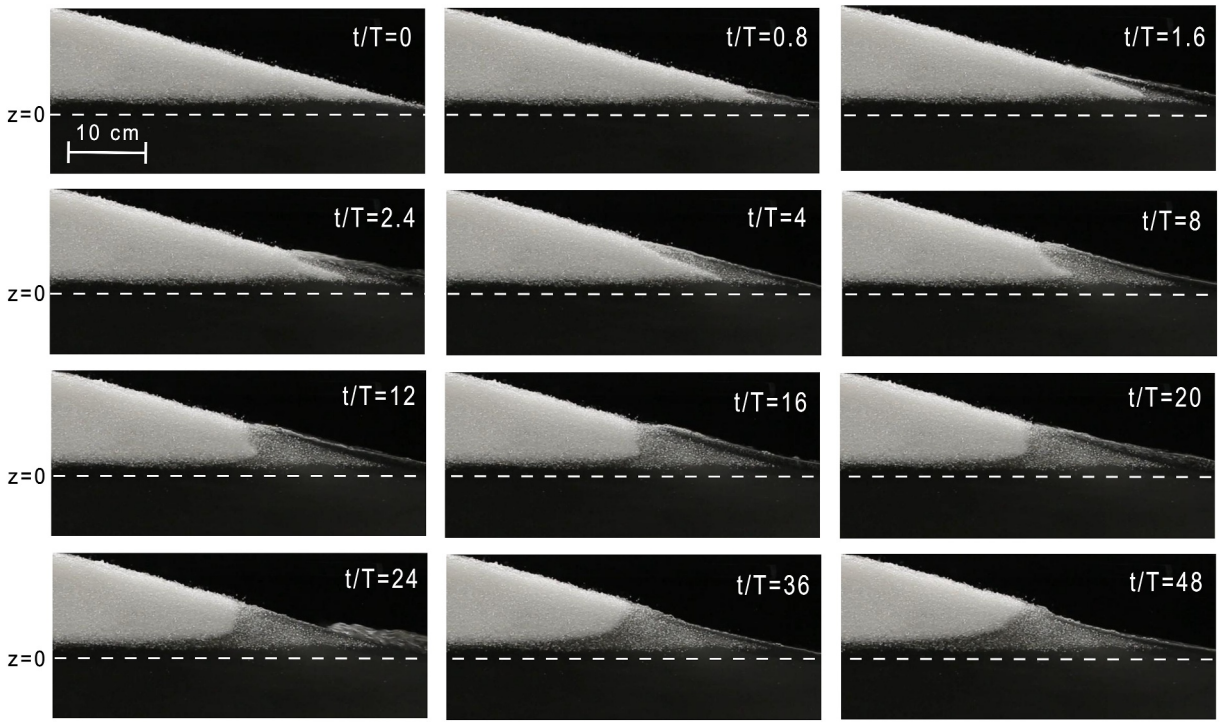

Figure 8. Unprocessed images showing evolution of the wetting front owing to a train of waves from $t/T = 0$ to 48 following wave arrival at the toe of the beach (not visible in $t/T = 0$) for test 15 (Table 1). Black areas indicate fully saturated sand, white areas indicate dry sand, and gray regions indicate areas of air entrapment within saturated pore space. The still fluid level ($z = 0$) is indicated by horizontal dashed lines.

For the same x_{Rp} (~24.5 cm), the 1:6 slope has only ~66% of the space between the beach face and still fluid level compared with the 1:4 slope, resulting in the 1:6 slope having a narrower vadose zone at $t = 0$ and less total infiltration capacity. The infiltration wedge that forms in the vadose zone reaches a steady state soon after the first wave, suggesting infiltration rates remain relatively constant for the remainder of the test. In contrast, the steeper slope experiences increased infiltration over the first 4–5 swash cycles while the infiltration wedge forms in the vadose zone, leading to reduced runup.

The shape of the wetting front is similar to prior observations (Austin & Masselink, 2006; Heiss et al., 2015), with both vertical infiltration downward in the upper swash and cross-shore infiltration that raises the groundwater table. Infiltration and drainage of fluid through the vadose zone toward the phreatic surface is slightly faster than in a lower permeability sandy beach ($t/T = 8$ here is comparable with $t/T = 15$, Heiss et al., 2015) and slower than in a higher permeability gravel beach ($t/T < 1.0$, Austin & Masselink, 2006). Hence, permeability impacts the relative rate of wetting front progression to form the infiltration wedge, confirming the findings of prior studies (Geng et al., 2017). Further, similarities between the present tests and previous studies suggest that the use of crushed quartz and mineral oil mixture used here are applicable proxies for sand and water.

3.3. Saturation Beyond the Swash Zone

Infiltration from the wave runup impacts the distal region of the subsurface ($x/x_{Rp} > 1.0$), as well as the swash zone. This distal region is influenced by the back wall boundary conditions. Back wall boundary conditions are varied to investigate how the confinement of a flume impacts subsurface fluid dynamics, while also illustrating how the wetting front interacts with horizontal movement of fluid into the beach. Onshore of the maximum runup ($x/x_{Rp} > 1.0$), the subsurface fluid elevation rises with time along the full extent of the flume. For tests with no flow between the head tank and the flume (closed valve), the total rise in fluid elevation decreases with distance from the mean shoreline. At locations of $1.0 < x/x_{Rp} < 2.0$ after infiltration wedge formation ($t/T > 16$ in Figure 8), the profile of the subsurface fluid initially is steep, sloping downwards in the cross-shore direction, to connect the edge of the infiltration wedge at $x/x_{Rp} = 1.0$ with the phreatic surface. As the wetting front progresses and the phreatic surface beyond the swash zone rises, the profile of fluid elevation in $2.0 > x/x_{Rp} > 1.0$ becomes less steep

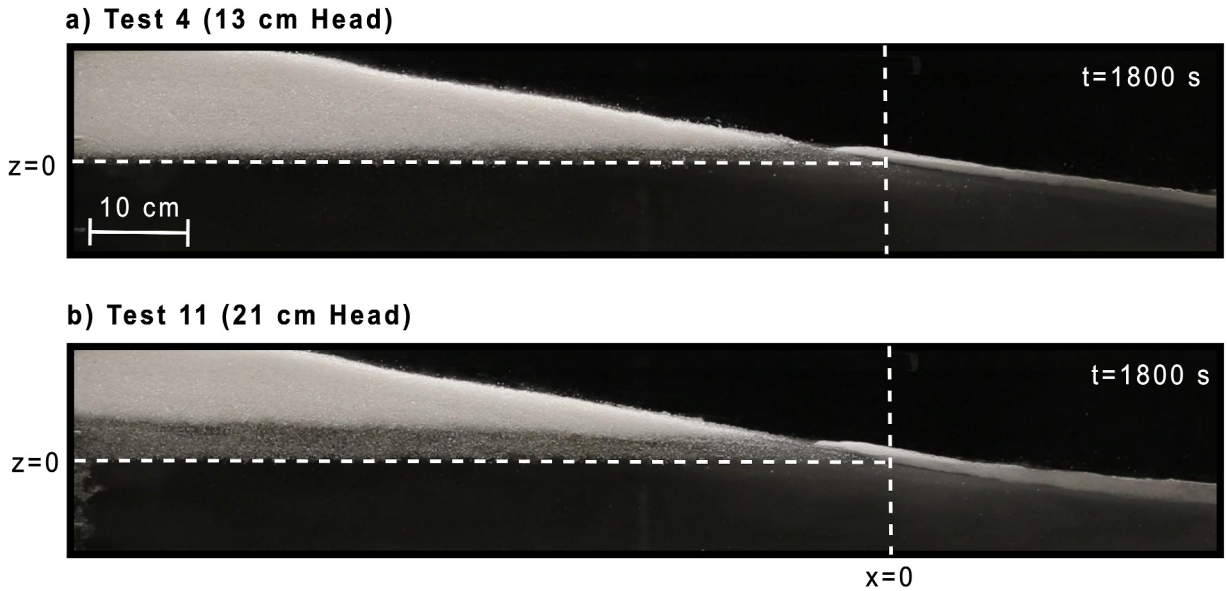

Figure 9. Unprocessed images showing the saturation rise at t = 1,800 s (t/T = 1,440) on a 1:6 beach slope for: (a) h = 13, and (b) h = 21 cm head at the back wall boundary. The still fluid level (z = 0) and the mean shoreline (x = 0) are indicated by dashed lines.

(e.g., t/T = 48 in Figure 8). The rate of fluid rise in regions of $x/x_{Rp} > 1.0$ is dependent on how quickly the runup-driven infiltrating fluid can flow laterally through the beach, as well as the hydraulic boundary condition applied at the back wall of the flume.

When the infiltration wedge in the subsurface of the swash zone reaches pore capacity (given air entrapment and dry porosity), fluid that enters the aquifer flows laterally through the swash zone subsurface, and toward the back wall of the flume. A closed valve prevents fluid from exiting from the back of the flume and the open valve enables exchanges between the head tank and the beach. Under closed valve conditions, fluid that would otherwise continue to flow cross-shore in a continuous aquifer accumulates at the back wall boundary. When the back wall boundary head condition is an open valve with h = 13 cm (Figure 9a), the rise in saturation elevation is minimal ($z < 1.5$ cm) because fluid can continue to flow out through the valve if the pore pressure in the head tank is less than the subsurface. Conversely, when the valve is open and the boundary head condition is $h > 13$ cm, exceeding the still fluid depth and the phreatic surface elevation, the total observed rise in saturation at the back of the beach is higher (up to z = 4.5 cm) due to fluid flowing into the flume from the head tank, which drives a positive, offshore-directed subsurface fluid gradient (Figure 9b). The volume of fluid that exits (h = 13 cm tests) or enters (h = 17 or 21 cm tests) the flume through the valve over the duration of each test ranges from 420 mL exiting the flume for the h = 13 cm test (<1% initial flume volume) to 1,290 mL entering the flume for the h = 21 cm test (2.5% initial flume volume).

Saturation elevation near the back wall (x/x_{Rp} = 4.0) has been quantified for triplicates (shaded areas in Figure 10). The subsurface fluid elevation does not vary with beach slope, although given the physical limitations of the slopes used, larger variations in bathymetry may show a more pronounced rise in saturation in the back of the beach. The initial elevation of fluid above the phreatic surface (t = 0 in Figure 10) varies by 0.1–1.0 cm for individual tests due to local variations in grain distribution. Subsurface fluid elevations align over time in tests with the same boundary conditions.

Tests that impose a closed (Figure 10a) or open (Figure 10b) valve with h = 13 cm at the boundary have more variability in the subsurface fluid elevation between triplicate tests than boundary conditions with heads exceeding the initial phreatic surface elevation ($h > d_0$) (Figures 10c and 10d). In tests with the closed valve or with h = 13 cm ($h = d_0$), fluid motion is dominated by swash driving infiltration onshore, either accumulating at the back wall or flowing out the valve, with minimal to no flow into the flume from the head tank. Under these boundary conditions, variable bulging (~1–2 cm) at the back wall can occur (indicated by the small changes in fluid elevation with time in Figures 10a and 10b). In cases with elevated head boundary conditions ($h > d_0$)

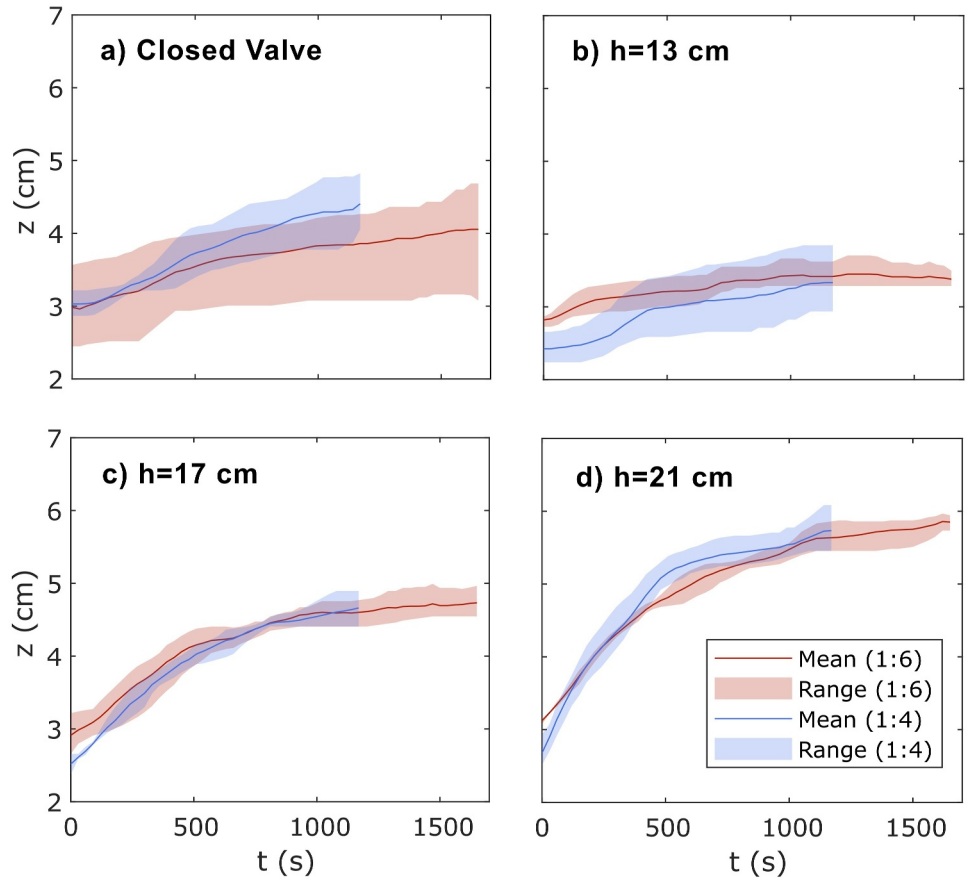

Figure 10. Fluid elevation (z) at $x/x_{Rp} = 4.0$ vs. time for each back wall boundary condition: (a) closed valve, (b) open valve with $h = 13$, (c) open valve with $h = 17$, and (d) open valve with $h = 21$ cm. Solid curves indicate the mean subsurface fluid elevation over three repeat tests and shading represents the range of elevations observed. Fluid elevations are estimated every 30 s, averaged over a width of five-pixels (3.5 mm), and smoothed using a lowpass moving average filter ($n = 5$) to reduce noise from short timescale wetting and drying.

(Figures 10c and 10d), offshore flow from the boundary interacts with onshore flow driven by the swash. Fluid elevations for $h > d_0$ boundary conditions vary less across triplicate tests and reach higher elevations by the end of the test.

3.4. Grain Size

One additional test using the fine-grained transparent sand is conducted to examine the impact of grain size variability on infiltration and subsurface saturation. The fine-grained transparent sand has a larger coefficient of uniformity ($Cu = 3.3$) than the coarse-grained sand ($Cu = 2.3$), though both are poorly graded. However, the median grain size of the fine material is significantly smaller ($D_{50} = 0.40$ mm) than the coarse-grained sand ($D_{50} = 1.70$ mm). The fine-grained material exhibits a larger capillary fringe (up to 8.5 cm) due to the smaller pore space between grains, as observed in previous studies (Taylor-Noonan et al., 2021). The initial capillary fringe extends to a higher elevation on the beach face than the wave runup elevation ($z > z_{Rp}$) and no wave-driven infiltration is observed (not shown). Additionally, high capillarity of the fine-grained sand results in an irregular initial phreatic surface elevation and shape that cannot be reproduced consistently.

Future work on the impact of grain size could be pursued by using a longer flume that can generate larger waves that result in a higher runup elevation that exceeds the capillary fringe elevation of the fine-grained sand. However, to observe air intrusion, interstitial air in the initially saturated subsurface must be removed as the beach is being constructed, which presents a practical limitation in the large-scale application of transparent sand unless

alternative approaches are used for air removal or initial air entrapment is neglected. Hence, increasing the scale of the experiments for fine-grained tests may be challenging.

4. Discussion

The application of transparent sand for subsurface flow investigation allows for the spatial discretization of the degree of saturation (S_r) at each pixel in every image. Beyond tracing the wetting front by changes in brightness (dry vs. saturated grains), air entrapment can be quantified by computing the fraction of pore volume occupied by the oil mixture and attributing all remaining occupancy to interstitial air. Pores that progressively saturate (S_r is increasing) indicate that air is being forced out by the infiltrating fluid (oil mixture), whereas regions that maintain a steady degree of saturation ($S_r > 0$) indicate that any encapsulated air cannot escape, and the pores have reached their fluid capacity. Spatial variations in the degree of saturation with time are indicative of fluid movement. Quantification of air entrapment and discrete changes in subsurface flows are properties that give insight into how surface runup infiltrates into a beach and saturates the subsurface, but are challenging to obtain in sand-water experiments or field studies.

4.1. Local Saturation Increases Due To Wave Runup

The degree of subsurface saturation (S_r) over 1,200 s is examined for a vertical stack of pixels above the still fluid level at $x/x_{Rp} = 3.0$ (Figure 11a) and $x/x_{Rp} = 1.5$ (Figure 11b). Data at each cross-shore location are averaged over five pixels in the x- and z-direction, representing the mean saturation over a region that is 3.5 mm wide and 3.5 mm high. Two thresholds are selected as saturation migration indicators representative of a mid-point of saturation progression ($S_r = 0.5$) and a lower limit of total saturation ($S_r = 0.8$) (vertical dashed lines in Figures 11a and 11b). The maximum subsurface fluid elevation surpassing each S_r threshold is compared with each other over time at $x/x_{Rp} = 3.0$ (Figures 11c) and 1.5 (Figure 11d). At the beach face, infiltration at the point of maximum runup ($x/x_{Rp} = 1.0$) begins when wave runup reaches an elevation of z_{Rp} (<10 s, Figure 5). Farther into the beach, at $x/x_{Rp} = 1.5$, the fluid elevation surpasses the S_r thresholds rapidly (between $t = 30$–300 s), after which they gradually reach steady-state (Figure 11d). At $x/x_{Rp} = 3.0$, farther from the swash zone, the elevations surpassing each S_r threshold follow a linear trend (Figure 11c). The initiation of the saturation progression at the $x/x_{Rp} = 3.0$ cross-shore location ($t = 60$ s) lags the response at $x/x_{Rp} = 1.5$ ($t = 30$ s). At both cross-shore locations, the rate of change in subsurface elevation surpassing S_r thresholds occurs over significantly longer time periods than at $x/x_{Rp} = 1.0$ and decreases over the duration of the test.

Similar analyses were attempted within the swash zone ($x/x_{Rp} \leq 1.0$), however, accurate values of S_r could not be computed in this regime due to variable lighting intensity. Image processing to determine the degree of saturation relies on consistent light intensity, provided in this case by ceiling located fluorescent lighting. However, below the continuous runup and run-down in the swash zone, light provided to the soil grains changes constantly. Thus, analyses of the subsurface in the swash zone focused on the readily observed and delineated wetting front migration, rather than quantifying the degree of saturation.

4.2. Dimensionless Subsurface Flows

Investigating local changes in S_r in a laboratory setting is useful for understanding subsurface air entrapment and fluid progression for application in field studies, where the cross-shore distance (i.e., 550 m in Housego et al., 2021) exceeds the dimensions of most laboratory experiments (3.62 m here). For comparison, experimental results can be non-dimensionalized. The maximum subsurface fluid elevations surpassing the selected S_r thresholds (Figures 11c and 11d) are scaled to a dimensionless parameter space (t/T, z/z_{Rp}, x/x_{Rp}) for four cross-shore locations on each beach slope (Figure 12). Each of the tests in the comparison has an imposed boundary head condition of $h = 13$ cm to approximate extreme surge conditions and an unconfined aquifer, potentially with a lagoon or depression enabling drainage at the inland end.

Subsurface fluid elevations (z/z_{Rp}) surpassing the $S_r = 0.5$ and 0.8 thresholds typically increase over time and eventually reach steady-state, with differences for different cross-shore-locations (x/x_{Rp}) and threshold values (Figure 12). At the onset of wave interaction with the beach slope ($t/T = 0$), the 50% saturation threshold ($S_r = 0.5$) is passed at a subsurface fluid elevation between $z/z_{Rp} = 0.40$–0.55 for all tests due to the capillary fringe above the still fluid level surface. At the higher $S_r = 0.8$ threshold, the subsurface fluid elevation is lower ($z/z_{Rp} = 0.30$–0.45), indicating the presence of air in the upper capillary fringe. For each test-threshold combination, z/z_{Rp}

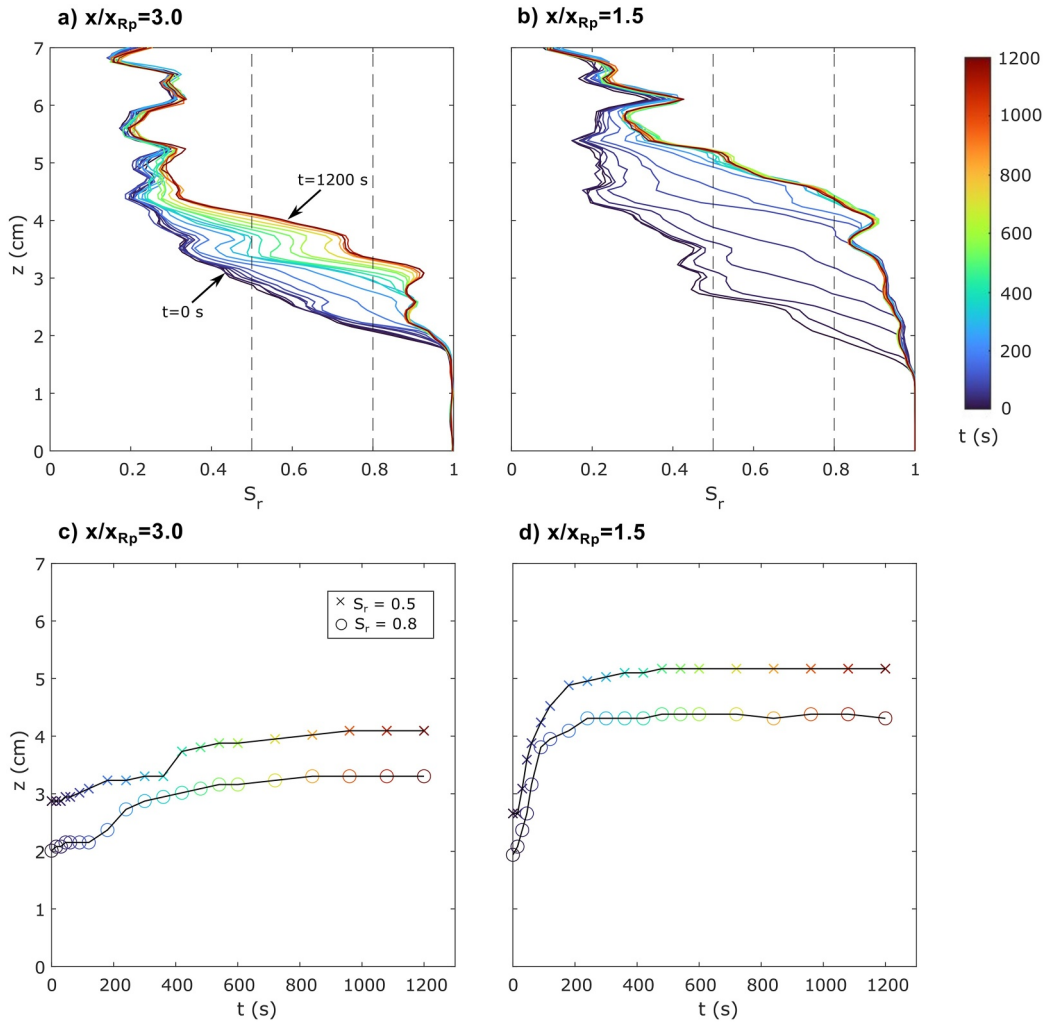

Figure 11. Vertical profiles of saturation above the still fluid level at relative cross-shore locations (a) $x/x_{Rp} = 3.0$, and (b) $x/x_{Rp} = 1.5$ for different times (colors, scale on right). Maximum elevation surpassing a threshold of $S_r = 0.5$ (crosses) and 0.8 (circles) pore saturation vs. time at relative cross-shore locations (c) $x/x_{Rp} = 3.0$, and (d) $x/x_{Rp} = 1.5$ for a 1:4 slope (test 18).

initially increases rapidly close to the swash zone (e.g., $x/x_{Rp} = 1.5$ in Figure 12), and increases gradually at locations farther from the swash zone (e.g., $x/x_R = 4.0$ in Figure 12). The difference in saturation rate (changes in z/z_{Rp} with time) indicates the lag in arrival time of fluid to distal regions in the subsurface. The elevation of the fluid in the subsurface at the end of the test ($t/T = 960$) is not the same at all cross shore-locations (observed in Figure 9). The difference between subsurface fluid elevations at cross-shore locations is more pronounced for tests on the steeper 1:4 slope. At some cross-shore locations (e.g., $x/x_{Rp} = 2.0$ and 3.0 in Figures 12a and 12c), the dimensionless subsurface fluid elevation response over time is different for each slope, based on different values of the initial capillary rise (z/z_{Rp} at $t/T = 0$).

The observations near the swash zone ($x/x_{Rp} = 1.5$) align with previous studies of saturation in the swash zone subsurface. For example, a study using moisture sensors on natural sandy beaches observed rapid increases in saturation at the beach face due to surface runup that propagated downwards toward the rising subsurface fluid elevation (Heiss et al., 2014). A "partially saturated" wetting front formed the infiltration wedge, indicative of $S_r < 1$ due to entrapped air within the swash zone subsurface (Heiss et al., 2014). Similar to the results here, volumetric water content in the subsurface initially was low and progressively increased over the testing duration, resulting in reduced water content fluctuations due to the decreasing available pore space.

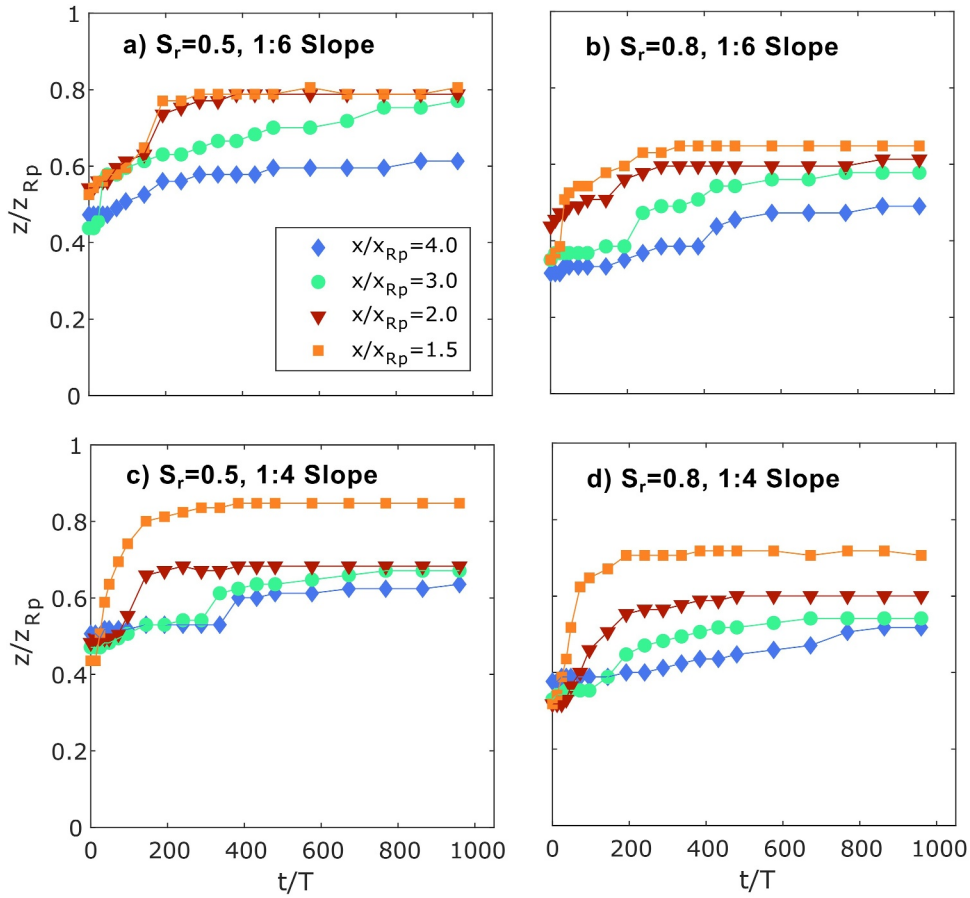

Figure 12. Non-dimensional vertical location of the maximum elevation (z/z_{Rp}) that surpasses a saturation threshold (S_r) versus relative time (t/T) for: (a) $S_r = 0.5$ on a 1:6 slope (test 4), (b) $S_r = 0.8$ on a 1:6 slope (test 4), (c) $S_r = 0.5$ on a 1:4 slope (test 18), and (d) $S_r = 0.8$ on a 1:4 slope (test 18). All the tests shown have the same boundary condition ($h = 13$ cm head).

4.3. Practical Applications

Previous field studies have collected observations of groundwater elevation changes due to wave runup or surge on permeable beaches. On Sable Island, NS, Canada, groundwater levels vertically increased by 1.6 m approximately 230 m away from the mean shoreline in response to a post-tropical storm (12 m offshore significant wave height) (Cantelon et al., 2023). In another study, a 1.0 m rise in the groundwater table was observed onshore of a dune on a sandy, barrier island beach following large, hurricane-driven waves and surge (Housego et al., 2021). Groundwater levels were elevated up to 310 m inland with a time-lagged response that decreased in amplitude with distance from the shoreline. Numerically modeled long-term impacts of the surface water-driven rises in groundwater included increased groundwater table elevations at cross-shore locations 300 m from the shoreline following a moderate (~0.8 m) increase in shoreline elevation over an 80 year simulation (Heiss et al., 2022).

The results of this study are consistent with prior field and laboratory observations (Housego et al., 2021; Turner et al., 2016; Yang et al., 2022) that showed "bulging" of fluid in the subsurface resulting from the combination of runup-driven infiltration and boundary conditions beyond the swash zone. The high-resolution observations of wetting front evolution presented here are similar to the infiltration pathways proposed for a natural gravel beach (Austin & Masselink, 2006). However, the lower beach permeability in the laboratory study here results in a persistent infiltration wedge and decoupling of the exit point and the free surface, similar to that in a sandy beach (Heiss et al., 2015). Previous work indicates asymmetric rises in onshore groundwater elevations time-lagged in response to surface wave runup, consistent with the present laboratory observations (Austin & Masselink, 2006; Housego et al., 2021; Nielsen, 1990). Tests that impose a boundary condition with a head tank elevation equal to

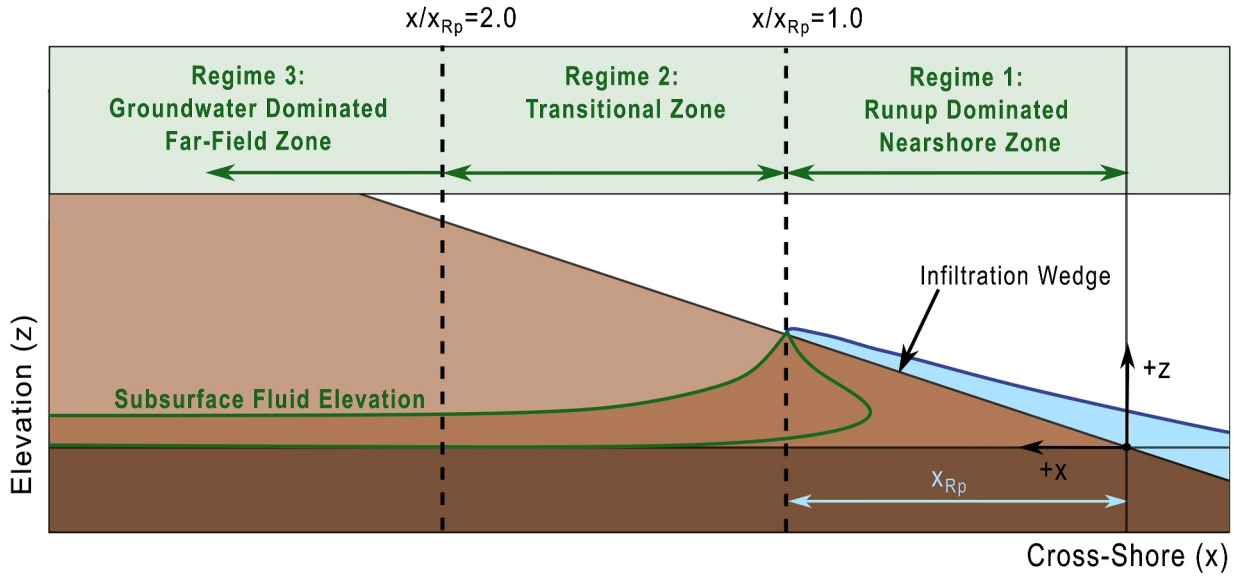

Figure 13. Conceptual model of subsurface fluid elevation regimes, including the runup dominated regime where the infiltration wedge forms within the nearshore zone (Regime 1, $x/x_{Rp} \leq 1.0$), the sloping transitional regime that decreases in elevation in the cross-shore direction (Regime 2, $2.0 < x/x_{Rp} < 1.0$), and the approximately flat, groundwater dominated regime in the far-field zone (Regime 3, $x/x_{Rp} \geq 2.0$). Subsurface fluid elevation profiles (green lines) are shown to indicate the general shape of the subsurface fluid elevation at different times.

the still surface fluid elevation may be the most similar to conditions during extreme waves (Housego et al., 2021), surges (Paldor et al., 2022), or tsunamis. Tests with elevated head tank boundary conditions are expected to be most consistent with natural beaches, whereas the closed valve tests would be representative of beaches with an impermeable retaining wall or structure in the backshore.

Comparison of fields with experimental observations is not trivial. Past studies have reported groundwater measurements at distal cross-shore locations that would exceed the $x/x_{Rp} = 4.0$ limit used here. Most importantly, field measurements refer to water flow through natural sand, whereas the present study uses a quartz sand and oil mixture. Transparent sand provides a useful way of visualizing fluid motion inside a laboratory beach, revealing the response time and length scales of a beach subsurface saturation fluctuations during wave forcing. However, validation with field observations is limited.

Similar to prior studies (Robinson, Gibbes, et al., 2007; Robinson, Li, & Barry, 2007; Santos et al., 2012, and many others), the fluid elevation in the subsurface of a beach includes a swash-driven flow region ($x/x_{Rp} \leq 1.0$) and an inland groundwater-driven region. Between these regions lies a transition zone (Figure 13). The saturation in the swash region is dominated by tide and wave runup driven infiltration and is highly dynamic during the formation of the infiltration wedge. For a sandy beach, the profile of the fluid elevation in this region is variable in shape and size over time, and transitions from dry to a steady state of saturation with entrapped air. Regime three is located in the far-field zone at $x/x_{Rp} \geq 2.0$ and is controlled by the coastal groundwater conditions. The subsurface fluid elevation in Regime three is relatively flat. The transitional zone, Regime 2, lies between the swash and groundwater regions at a cross-shore distance of $2.0 < x/x_{Rp} < 1.0$. Similar to prior laboratory studies (Turner et al., 2016), the groundwater table exhibits a distinct downward slope in the shoreward direction in this region to connect the fluid elevation profiles of Regime 1 and Regime 3. The relative slope of the fluid elevation profile in this region changes over time, transitioning from steep to flat as swash infiltrates cross-shore. The observations here may be comparable with a high tide or storm-type behavior in a natural swash zone.

5. Conclusions

A series of laboratory wave flume experiments were conducted using transparent sand and an optically matched fluid to measure the spatiotemporal variability in subsurface saturation of a beach subjected to surface gravity waves. The experiments used crushed quartz and oil as a proxy for sand and water to investigate how wave runup drives fluid motion in the subsurface. Beach slope and back wall boundary conditions were varied for

monochromatic waves, still fluid level, and grain size. A new technique is demonstrated to measure surface wave-driven subsurface saturation with high spatial resolution without installing sensors inside the aquifer.

Consistent with prior studies (Heiss et al., 2015; Yang et al., 2022), but with significantly higher spatial density of observations, the results show the rapid progression of a wave runup-driven infiltration wedge in the initially unsaturated subsurface of the swash zone, followed by a time lagged rise in saturation near the back of the beach. Runup elevation on the beach face is impacted by the progressive subsurface saturation directly below the runup zone, as well as the beach slope. The fluid elevation inside the granular beach is dependent on runup elevation, as well as the back wall boundary conditions.

The change in the maximum elevation of pore saturation that crosses selected degrees of saturation thresholds has a similar trend across tests and increases more rapidly at cross-shore distances closer in proximity to the swash zone. When scaled into dimensionless parameters, the relationship between runup properties and the subsurface response was different for each beach slope, including the initial pore fluid elevations due to capillary rise. The time-lagged and asymmetric vertical rise in the subsurface fluid level reaches equilibrium over time and fluid is more elevated at the end of the test for the steeper slope. The experimental results were used to present a conceptual model of subsurface fluid regimes that describes expected groundwater profiles for different relative cross-shore locations, including a transitional zone that separates the groundwater- and runup-dominated regions. Overall, the results of this experimental study using transparent sand provide a new and detailed view of subsurface fluid flow driven by surface wave runup.

Data Availability Statement

The observations used in this study are archived in the Groundwater Hydrodynamic Oscillations from Swash with Transparent Sand (GHOSTS) Borealis Data repository at Queen's University. Data is publicly accessible with the DOI: https://doi.org/10.5683/SP3/OYQ579.

Acknowledgments
We thank Kristine Mattson at the Royal Military College of Canada, and Anna Bryan and Dawson Ethier at Queen's University for help with the laboratory experiments. Funding for this research was provided by Natural Sciences and Engineering Research Council of Canada (NSERC) under the Discovery Grant programs awarded to G.A Siemens (RGPIN-2018-04373) and R.P. Mulligan (RGPIN-2024-04097). M.P. Delisle is supported by the Francis E. Fowler IV Fund at the Woods Hole Oceanographic Institution. B. Raubenheimer and S. Elgar acknowledge funding from the Earth Sciences (EAR) and Physical Oceanography (PO) programs of the US National Science Foundation (NSF).

References

Adams, K. H., Reager, J. T., Rosen, P., Wiese, D. N., Farr, T. G., Rao, S., et al. (2022). Remote sensing of groundwater: Current capabilities and future directions. *Water Resources Research*, *58*(10), e2022WR032219. https://doi.org/10.1029/2022wr032219

Austin, M. J., & Masselink, G. (2006). Swash–groundwater interaction on a steep gravel beach. *Continental Shelf Research*, *26*(20), 2503–2519. https://doi.org/10.1016/j.csr.2006.07.031

Bakhtyar, R., Brovelli, A., Barry, D. A., & Li, L. (2011). Wave-induced water table fluctuations, sediment transport and beach profile change: Modeling and comparison with large-scale laboratory experiments. *Coastal Engineering*, *58*(1), 103–118. https://doi.org/10.1016/j.coastaleng.2010.08.004

Bond, H., Wengrove, M., Puleo, J., Pontiki, M., Evans, T. M., & Feagin, R. A. (2023). Beach and dune subsurface hydrodynamics and their influence on the formation of dune scarps. *Journal of Geophysical Research: Earth Surface*, *128*(12), e2023JF007298. https://doi.org/10.1029/2023jf007298

Boufadel, M. C., Li, H., Suidan, M. T., & Venosa, A. D. (2007). Tracer studies in a laboratory beach subjected to waves. *Journal of Environmental Engineering*, *133*(7), 722–732. https://doi.org/10.1061/(asce)0733-9372(2007)133:7(722)

Butt, T., Russell, P., & Turner, I. (2001). The influence of swash infiltration–exfiltration on beach face sediment transport: Onshore or offshore? *Coastal Engineering*, *42*(1), 35–52. https://doi.org/10.1016/s0378-3839(00)00046-6

Cantelon, J. A., Guimond, J. A., Robinson, C. E., Michael, H. A., & Kurylyk, B. L. (2022). Vertical saltwater intrusion in coastal aquifers driven by episodic flooding: A review. *Water Resources Research*, *58*(11), e2022WR032614. https://doi.org/10.1029/2022wr032614

Cantelon, J. A., Robinson, C. E., & Kurylyk, B. L. (2023). Morphologic, atmospheric, and oceanic drivers cause multi-temporal saltwater intrusion on a remote, sand island. *Water Resources Research*, *59*(10), e2023WR035820. https://doi.org/10.1029/2023wr035820

Cartwright, N., Li, L., & Nielsen, P. (2004). Response of the salt–freshwater interface in a coastal aquifer to a wave-induced groundwater pulse: Field observations and modelling. *Advances in Water Resources*, *27*(3), 297–303. https://doi.org/10.1016/j.advwatres.2003.12.005

Conley, D. C., & Inman, D. L. (1994). Ventilated oscillatory boundary layers. *Journal of Fluid Mechanics*, *273*, 261–284. https://doi.org/10.1017/s002211209400193x

Constantz, J., Herkelrath, W. N., & Murphy, F. (1988). Air encapsulation during infiltration. *Soil Science Society of America Journal*, *52*(1), 10–16. https://doi.org/10.2136/sssaj1988.03615995005200010002x

Delisle, M. P. C., Gallien, T. W., & Kim, Y. (2023). A numerical study of dam-break driven swash and beach groundwater interactions. *Journal of Geophysical Research: Oceans*, *128*(9), e2022JC019615. https://doi.org/10.1029/2022jc019615

Duncan, J. R., Jr. (1964). The effects of water table and tide cycle on swash-backwash sediment distribution and beach profile development. *Marine Geology*, *2*(3), 186–197. https://doi.org/10.1016/0025-3227(64)90039-8

Ezzein, F., & Bathurst, R. (2011). A transparent sand for geotechnical laboratory modeling. *Geotechnical Testing Journal*, *34*(6), 590–601. https://doi.org/10.1520/gtj103808

Faybishenko, B. A. (1995). Hydraulic behavior of quasi-saturated soils in the presence of entrapped air: Laboratory experiments. *Water Resources Research*, *31*(10), 2421–2435. https://doi.org/10.1029/95wr01654

Florence, M., Stark, N., Raubenheimer, B., & Elgar, S. (2022). Nearshore vertical pore pressure gradients and onshore sediment transport under tropical storm forcing. *Journal of Waterway, Port, Coastal, and Ocean Engineering*, *148*(6), 04022023. https://doi.org/10.1061/(asce)ww.1943-5460.0000723

Ganiyu, A. A., Rashid, A. S. A., & Osman, M. H. (2016). Utilisation of transparent synthetic soil surrogates in geotechnical physical models: A review. *Journal of Rock Mechanics and Geotechnical Engineering*, *8*(4), 568–576. https://doi.org/10.1016/j.jrmge.2015.11.009

Gast, R. J., Elgar, S., & Raubenheimer, B. (2015). Observations of transport of bacterial-like microspheres through beach sand. *Continental Shelf Research*, *97*, 1–6. https://doi.org/10.1016/j.csr.2015.01.010

Geng, X., Heiss, J. W., Michael, H. A., & Boufadel, M. C. (2017). Subsurface flow and moisture dynamics in response to swash motions: Effects of beach hydraulic conductivity and capillarity. *Water Resources Research*, *53*(12), 10317–10335. https://doi.org/10.1002/2017wr021248

Geng, X., Heiss, J. W., Michael, H. A., Boufadel, M. C., & Lee, K. (2020). Groundwater flow and moisture dynamics in the swash zone: Effects of heterogeneous hydraulic conductivity and capillarity. *Water Resources Research*, *56*(11), e2020WR028401. https://doi.org/10.1029/2020wr028401

Geng, X., Heiss, J. W., Michael, H. A., Li, H., Raubenheimer, B., & Boufadel, M. C. (2021). Geochemical fluxes in sandy beach aquifers: Modulation due to major physical stressors, geologic heterogeneity, and nearshore morphology. *Earth-Science Reviews*, *221*, 103800. https://doi.org/10.1016/j.earscirev.2021.103800

Grant, U. S. (1948). Influence of the water table on beach aggradation and degradation. *Journal of Marine Research*, *7*, 655–660.

Heiss, J. W., Mase, B., & Shen, C. (2022). Effects of future increases in tidal flooding on salinity and groundwater dynamics in coastal aquifers. *Water Resources Research*, *58*(12), e2022WR033195. https://doi.org/10.1029/2022wr033195

Heiss, J. W., Puleo, J. A., Ullman, W. J., & Michael, H. A. (2015). Coupled surface-subsurface hydrologic measurements reveal infiltration, recharge, and discharge dynamics across the swash zone of a sandy beach. *Water Resources Research*, *51*(11), 8834–8853. https://doi.org/10.1002/2015wr017395

Heiss, J. W., Ullman, W. J., & Michael, H. A. (2014). Swash zone moisture dynamics and unsaturated infiltration in two sandy beach aquifers. *Estuarine, Coastal and Shelf Science*, *143*, 20–31. https://doi.org/10.1016/j.ecss.2014.03.015

Horn, D. P. (2002). Beach groundwater dynamics. *Geomorphology*, *48*(1–3), 121–146. https://doi.org/10.1016/s0169-555x(02)00178-2

Horn, D. P. (2006). Measurements and modelling of beach groundwater flow in the swash-zone: A review. *Continental Shelf Research*, *26*(5), 622–652. https://doi.org/10.1016/j.csr.2006.02.001

Housego, R., Raubenheimer, B., Elgar, S., Cross, S., Legner, C., & Ryan, D. (2021). Coastal flooding generated by ocean wave-and surge-driven groundwater fluctuations on a sandy barrier island. *Journal of Hydrology*, *603*, 126920. https://doi.org/10.1016/j.jhydrol.2021.126920

Kang, H. Y., Nielsen, P., & Hanslow, D. J. (1994). Watertable overheight due to wave runup on a sandy beach. *Coastal Engineering*, *1994*, 2115–2124. https://doi.org/10.1061/9780784400890.154

Kikkert, G. A., Pokrajac, D., O'Donoghue, T., & Steenhauer, K. (2013). Experimental study of bore-driven swash hydrodynamics on permeable rough slopes. *Coastal Engineering*, *79*, 42–56. https://doi.org/10.1016/j.coastaleng.2013.04.008

Li, L., Barry, D. A., Parlange, J. Y., & Pattiaratchi, C. B. (1997). Beach water table fluctuations due to wave run-up: Capillarity effects. *Water Resources Research*, *33*(5), 935–945. https://doi.org/10.1029/96wr03946

Li, Y., & Raichlen, F. (2001). Solitary wave runup on plane slopes. *Journal of Waterway, Port, Coastal, and Ocean Engineering*, *127*(1), 33–44. https://doi.org/10.1061/(asce)0733-950x(2001)127:1(33)

Luijendijk, A., Hagenaars, G., Ranasinghe, R., Baart, F., Donchyts, G., & Aarninkhof, S. (2018). The state of the world's beaches. *Scientific Reports*, *8*(1), 6641. https://doi.org/10.1038/s41598-018-24630-6

Masselink, G., & Li, L. (2001). The role of swash infiltration in determining the beachface gradient: A numerical study. *Marine Geology*, *176*(1–4), 139–156. https://doi.org/10.1016/s0025-3227(01)00161-x

Munson, B. R., Young, D. F., & Okiishi, T. H. (1998). *Fundamentals of fluid mechanics* (p. 19). John Wiley and Sons.

Nielsen, P. (1990). Tidal dynamics of the water table in beaches. *Water Resources Research*, *26*(9), 2127–2134. https://doi.org/10.1029/wr026i009p02127

Nielsen, P. (1999). Groundwater dynamics and salinity in coastal barriers. *Journal of Coastal Research*, 732–740.

Packwood, A. R. (1983). The influence of beach porosity on wave uprush and backwash. *Coastal Engineering*, *7*(1), 29–40. https://doi.org/10.1016/0378-3839(83)90025-x

Paldor, A., Stark, N., Florence, M., Raubenheimer, B., Elgar, S., Housego, R., et al. (2022). Coastal topography and hydrogeology control critical groundwater gradients and potential beach surface instability during storm surges. *Hydrology and Earth System Sciences*, *26*(23), 5987–6002. https://doi.org/10.5194/hess-26-5987-2022

Peters, S. B., Siemens, G., & Take, W. A. (2011). Characterization of transparent soil for unsaturated applications. *Geotechnical Testing Journal*, *34*(5), 445–456. https://doi.org/10.1520/gtj103580

Raubenheimer, B., & Guza, R. T. (1996). Observations and predictions of run-up. *Journal of Geophysical Research*, *101*(C11), 25575–25587. https://doi.org/10.1029/96jc02432

Robinson, C., Gibbes, B., Carey, H., & Li, L. (2007). Salt-freshwater dynamics in a subterranean estuary over a spring-neap tidal cycle. *Journal of Geophysical Research*, *112*(C9). https://doi.org/10.1029/2006jc003888

Robinson, C., Gibbes, B., & Li, L. (2006). Driving mechanisms for groundwater flow and salt transport in a subterranean estuary. *Geophysical Research Letters*, *33*(3). https://doi.org/10.1029/2005gl025247

Robinson, C., Li, L., & Barry, D. A. (2007). Effect of tidal forcing on a subterranean estuary. *Advances in Water Resources*, *30*(4), 851–865. https://doi.org/10.1016/j.advwatres.2006.07.006

Robinson, C., Xin, P., Li, L., & Barry, D. A. (2014). Groundwater flow and salt transport in a subterranean estuary driven by intensified wave conditions. *Water Resources Research*, *50*(1), 165–181. https://doi.org/10.1002/2013wr013813

Santos, I. R., Eyre, B. D., & Huettel, M. (2012). The driving forces of porewater and groundwater flow in permeable coastal sediments: A review. *Estuarine, Coastal and Shelf Science*, *98*, 1–15. https://doi.org/10.1016/j.ecss.2011.10.024

Siemens, G. A., & Beddoe, R. A. (2017). Spatial resolution of degree of saturation measurements in unsaturated transparent soil experiments. *PanAm Unsaturated Soils*, *2017*, 174–184.

Siemens, G. A., Take, W. A., & Peters, S. B. (2014). Physical and numerical modeling of infiltration including consideration of the pore-air phase. *Canadian Geotechnical Journal*, *51*(12), 1475–1487. https://doi.org/10.1139/cgj-2013-0447

Sills, L. A. K., Mumford, K. G., & Siemens, G. A. (2017). Quantification of fluid saturations in transparent porous media. *Vadose Zone Journal*, *16*(2), 1–9. https://doi.org/10.2136/vzj2016.06.0052

Sous, D., Lambert, A., Rey, V., & Michallet, H. (2013). Swash–groundwater dynamics in a sandy beach laboratory experiment. *Coastal Engineering*, *80*, 122–136. https://doi.org/10.1016/j.coastaleng.2013.05.006

Steenhauer, K., Pokrajac, D., O'Donoghue, T., & Kikkert, G. A. (2011). Subsurface processes generated by bore-driven swash on coarse-grained beaches. *Journal of Geophysical Research*, *116*(C4), C04013. https://doi.org/10.1029/2010jc006789

Stockdon, H. F., Holman, R. A., Howd, P. A., & Sallenger, A. H., Jr. (2006). Empirical parameterization of setup, swash, and runup. *Coastal Engineering*, *53*(7), 573–588. https://doi.org/10.1016/j.coastaleng.2005.12.005

Taylor-Noonan, A. M., Siemens, G. A., Cabrera, M. A., Arpin, N. M., Parera Morales, F., & Take, W. A. (2021). Stability of saturated granular columns: Role of stress-dilatancy and capillarity. *Physics of Fluids*, *33*(3). https://doi.org/10.1063/5.0035029

Turner, I. L., & Masselink, G. (1998). Swash infiltration-exfiltration and sediment transport. *Journal of Geophysical Research*, *103*(C13), 30813–30824. https://doi.org/10.1029/98jc02606

Turner, I. L., Rau, G. C., Austin, M. J., & Andersen, M. S. (2016). Groundwater fluxes and flow paths within coastal barriers: Observations from a large-scale laboratory experiment (BARDEX II). *Coastal Engineering*, *113*, 104–116. https://doi.org/10.1016/j.coastaleng.2015.08.004

van Gent, M. R. (1994). The modelling of wave action on and in coastal structures. *Coastal Engineering*, *22*(3–4), 311–339. https://doi.org/10.1016/0378-3839(94)90041-8

Wada, Y., Lo, M. H., Yeh, P. J. F., Reager, J. T., Famiglietti, J. S., Wu, R. J., & Tseng, Y. H. (2016). Fate of water pumped from underground and contributions to sea-level rise. *Nature Climate Change*, *6*(8), 777–780. https://doi.org/10.1038/nclimate3001

Waddell, E. (1976). Swash – Groundwater – beach profile interactions. In R. A. Davis & R. L. Etherington (Eds.), *Beach and nearshore sedimentation* (Vol. 24, pp. 115–125). SEPM Special Publication. https://doi.org/10.2110/pec.76.24.0115

Waska, H., Greskowiak, J., Ahrens, J., Beck, M., Ahmerkamp, S., Böning, P., et al. (2019). Spatial and temporal patterns of pore water chemistry in the inter-tidal zone of a high energy beach. *Frontiers in Marine Science*, *6*, 154. https://doi.org/10.3389/fmars.2019.00154

Werner, A. D., Bakker, M., Post, V. E., Vandenbohede, A., Lu, C., Ataie-Ashtiani, B., et al. (2013). Seawater intrusion processes, investigation and management: Recent advances and future challenges. *Advances in Water Resources*, *51*, 3–26. https://doi.org/10.1016/j.advwatres.2012.03.004

White, D. J., Take, W. A., & Bolton, M. D. (2003). Soil deformation measurement using particle image velocimetry (PIV) and photogrammetry. *Géotechnique*, *53*(7), 619–631. https://doi.org/10.1680/geot.53.7.619.37383

Yang, M., Zheng, Y., & Liu, H. (2022). Experimental study of the solitary wave induced groundwater hydrodynamics. *Coastal Engineering*, *177*, 104193. https://doi.org/10.1016/j.coastaleng.2022.104193

Zheng, Y., Yang, M., & Liu, H. (2023). Does the capillary fringe account for the zero-phase lag phenomenon in the propagation of the wave-induced water table fluctuation in a coastal aquifer? *Coastal Engineering*, *182*, 104300. https://doi.org/10.1016/j.coastaleng.2023.104300